Modeling compliant bistable mechanisms: An energy method based on the high-order smooth curvature model

Tinghao Liu, Guangbo Hao, Jiaxiang Zhu, Pongsiri Kuresangsai, Salih Abdelaziz, Erich Wehrle

▶ To cite this version:

Tinghao Liu, Guangbo Hao, Jiaxiang Zhu, Pongsiri Kuresangsai, Salih Abdelaziz, et al.. Modeling compliant bistable mechanisms: An energy method based on the high-order smooth curvature model. International Journal of Mechanical Sciences, In press. lirmm-04555400

HAL Id: lirmm-04555400
https://hal-lirmm.ccsd.cnrs.fr/lirmm-04555400
Submitted on 22 Apr 2024

Modeling compliant bistable mechanisms: An energy method based on high-order smooth curvature model

SCME method:

(1) Define target trajectory points

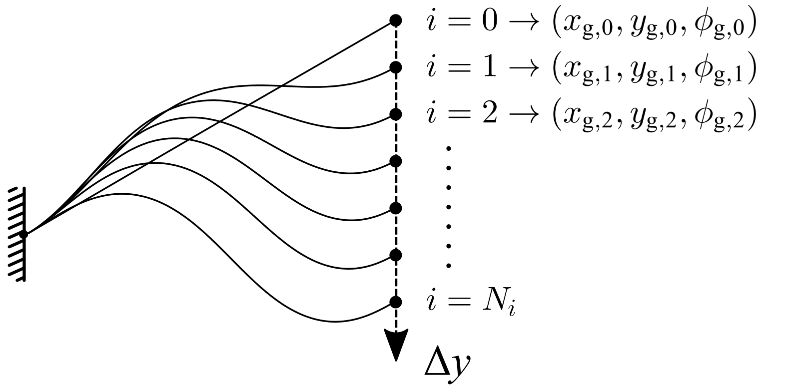

(2) Determining the beam configuration with the minimum bending strain energy, formulated using alpha as variables, through the application of the Lagrange multiplier method.

$$\mathcal{L}(\boldsymbol{\alpha},\boldsymbol{\lambda}) = U_{\mathrm{b}}(\boldsymbol{\alpha}) + \begin{bmatrix}\lambda_1 & \lambda_2 & \lambda_3\end{bmatrix}\begin{bmatrix} x_{\mathrm{g}} - x_{\mathrm{tip}}(\boldsymbol{\alpha}) \\ y_{\mathrm{g}} - y_{\mathrm{tip}}(\boldsymbol{\alpha}) \\ \phi_{\mathrm{g}} - \phi_{\mathrm{tip}}(\boldsymbol{\alpha}) \end{bmatrix}$$

(3) Derive the kinetostatic model based on the obtained generalized coordinates $\boldsymbol{\alpha}$ and Lagrange multiplier $\boldsymbol{\lambda}$. The beam curvature is derived based on generalized coordinates **α**, while the applied force and moment are derived using $\boldsymbol{\lambda}$.

Result Verification

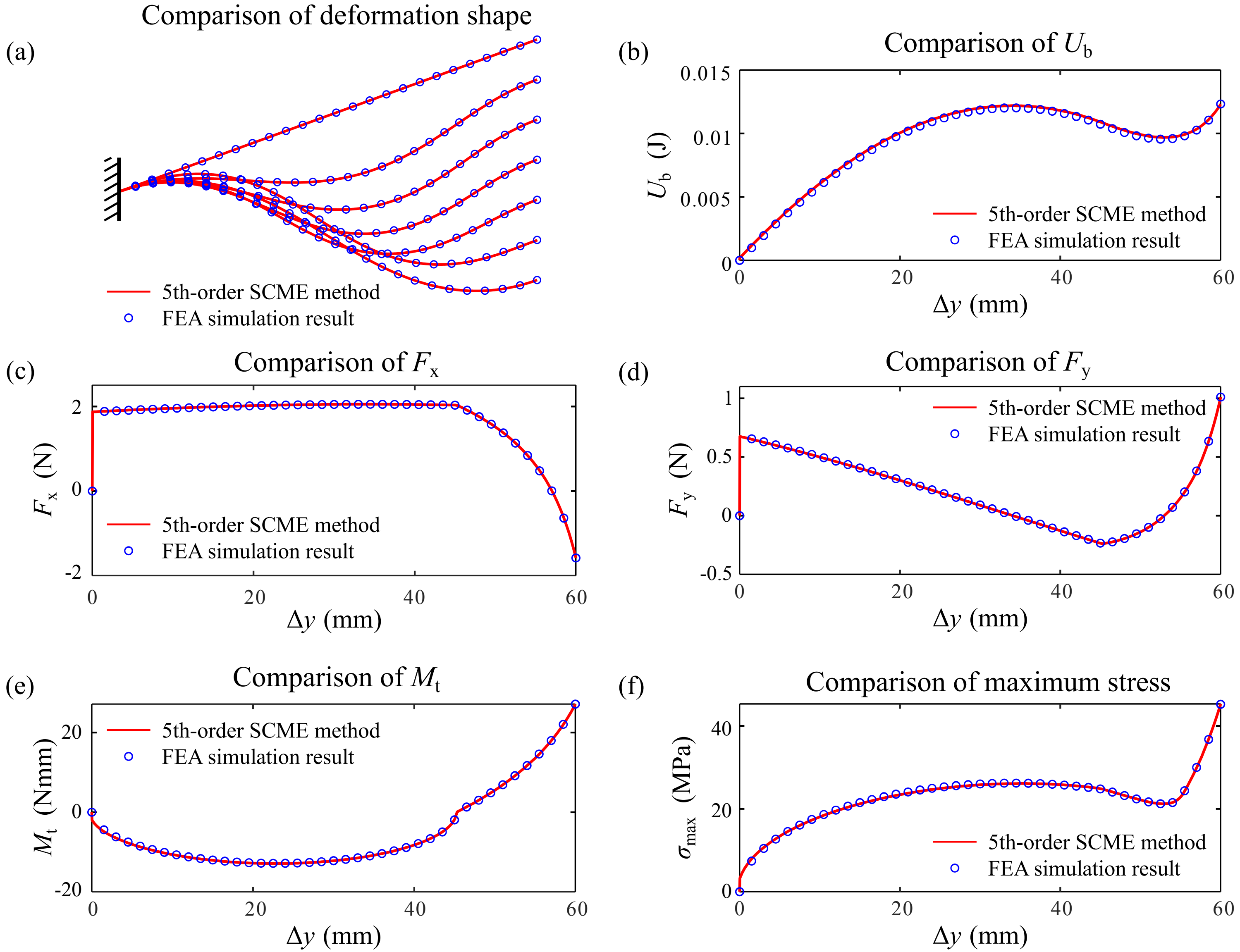

Comparative analysis

Accuracy comparison

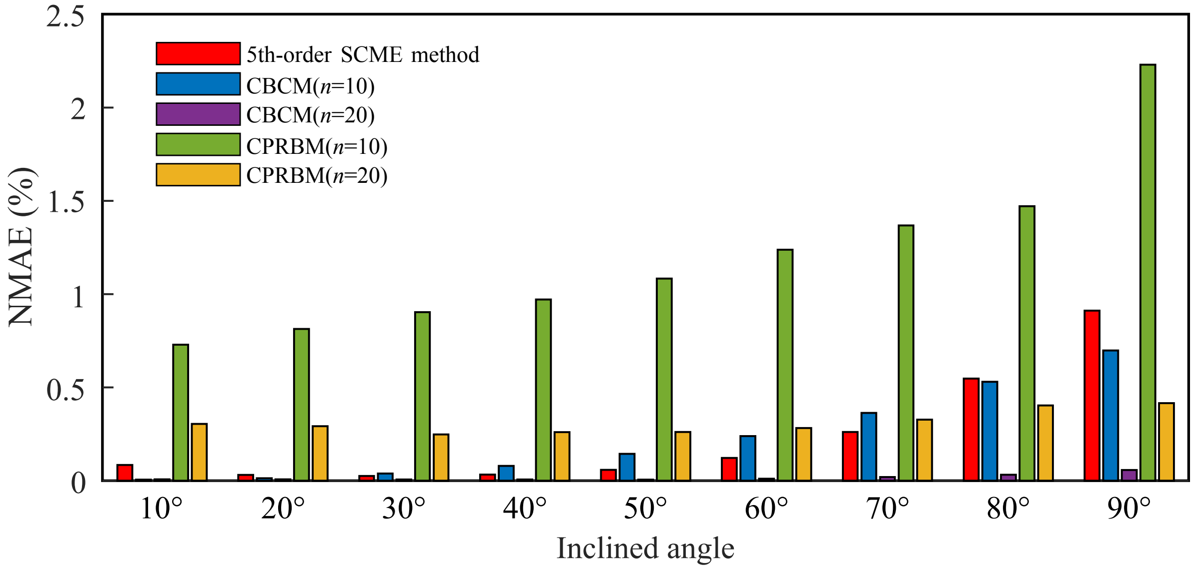

Computational efficiency comparison

when the trajectory has 200 sampling points ($N_i = 200$)

Inclined angle (θ)	10°	20°	30°	40°	50°	60°	70°	80°	90°
SCME method	0.075	0.074	0.079	0.081	0.085	0.096	0.105	0.111	0.097
FEA simulation	64	66	86	74	68	74	77	69	94
CBCM (n=10)	23.166	23.712	24.768	23.614	24.291	25.889	24.267	22.996	21.794
CBCM (n=20)	56.013	58.814	59.699	59.712	56.023	59.015	59.462	62.535	56.043
CPRBM (n=10)	11.946	11.892	11.794	11.193	11.463	11.497	11.062	10.953	10.934
CPRBM (n=20)	20.107	21.451	21.328	20.842	20.646	20.872	21.133	20.773	18.922

Measured in seconds

Highlights

Modeling compliant bistable mechanisms: An energy method based on the high-order smooth curvature model

Tinghao Liu, Guangbo Hao, Jiaxiang Zhu, Pongsiri Kuresangsai, Salih ABDELAZIZ, Erich Wehrle

- Accurate and comprehensive nonlinear large-deflection modeling via the SCME method.
- Efficient modeling capability without discretization.
- Application to full inclined angles from 0 to 90 degrees.
- Extensive comparisons with existing models, FEA and experiments.

Modeling compliant bistable mechanisms: An energy method based on the high-order smooth curvature model

Tinghao Liu[a], Guangbo Hao[a,*], Jiaxiang Zhu[a], Pongsiri Kuresangsai[b], Salih ABDELAZIZ[a,c], Erich Wehrle[d]

[a] *School of Engineering and Architecture, University College Cork, College Road, Cork, T12 K8AF, Ireland*
[b] *Department of Mechanical Engineering, Chiang Mai University, Chiang Mai, 50200, Thailand*
[c] *LIRMM, University of Montpellier, Montpellier, 34090, France*
[d] *Applied Research & Technology, Collins Aerospace, Munich, 80805, Germany*

Abstract

This paper applies an energy method based on the high-order smooth curvature model to address the challenges of kinetostatically modeling the complicated nonlinear post-buckling behavior of inclined compliant beams. The proposed energy method is grounded in the principle of minimum strain energy, implying that the total strain energy is minimized at the equilibrium configuration. In this work, the high-order smooth curvature model is adopted to accurately model the bending strain energy of large deformation beams. Subsequently, the Lagrange multiplier method is employed to ascertain the minimum of strain energy while concurrently determining the corresponding tip loads. Additionally, the deformation shape and maximum stress are determined via the smooth curvature model. The proposed method is introduced for the first time in modeling compliant bistable mechanisms, and it is proven that the method can be used for modeling compliant beams with inclined angles ranging from 0 to 90 degrees. Following the modeling, finite element analysis and experimental tests are conducted to verify the accuracy of the proposed energy method. A comprehensive comparative analysis between proposed method and existing methods is conducted. The comparison results prove that the model is more computationally efficient without compromising modeling accuracy The proposed modeling method can not only be used for modeling compliant bistable mechanisms but also has extendable applications in modeling initially-curved compliant beams, contact-aid design problems, and distributed load problems.

Keywords: Compliant bistable mechanisms, Smooth curvature model, Minimum strain energy method

---

1. Introduction

Compliant mechanisms, which rely on the deformation of compliant beams instead of traditional kinematic joints, have emerged as a significant area of interest in engineering [1]. They find application in various fields, including compliant grippers [2, 3], actuators [4], continuum robots [5, 6], origami mechanisms [7], morphing wings [8, 9] and deployable structures [10, 11]. Bistable mechanisms, a subset of compliant mechanisms, have gained special attentions due to their unique property of maintaining two stable states with zero power consumption. This feature makes them highly relevant in diverse areas such as energy harvesting [12–14], micro-electromechanical systems (MEMS) [15–17], morphing structures [18], deployable structures [19], multistable mechanisms [20, 21], and mechanical metamaterials [22–27].

Modeling compliant bistable mechanisms requires to address inherent nonlinearity stemming from large deformations [28]. Accurately modeling these nonlinear behaviors proves challenging, particularly given the buckled beam. Creating simplified and computationally efficient models becomes a promising task in light of these complexities. To address this gap, this paper aims to propose an alternative energy approach for modeling large deformation beams in

---

[*] Corresponding Author
Email address: `G.Hao@ucc.ie` (Guangbo Hao)
URL: `https://sites.google.com/site/doctorghao/` (Guangbo Hao)

compliant bistable mechanisms. The proposed energy method can accurately model the deformation shape, applied force and moment, strain energy and stress in compliant bistable mechanisms.

Numerical methods, such as finite element analysis (FEA), are often necessary, but can be computationally expensive [29]. In prior studies, numerous modeling methods have been proposed for the analysis of compliant mechanisms. These methods can be broadly categorized into four main categories: smooth curvature model (SCM) [30], pseudo-rigid-body model (PRBM) [31], beam constraint model (BCM) [32, 33], and elliptic integral solution (EIS) [34]. The majority of compliant mechanisms have been subjected to modeling, analysis, and optimization using these four fundamental methods and their respective branch methods. The application of these approaches has significantly advanced the development of compliant mechanisms. In the following content, we will conduct an in-depth review of the strengths and weaknesses of these methods.

The pseudo-rigid-body model (PRBM) employs rigid-body components with equivalent force-deflection characteristics to predict system deflection and force-deflection relationships. The 1R-PRBM consists of two rigid links joined at a pin joint and a torsion spring along the beam [31, 35, 36]. However, the approximation error becomes significantly large when the tip inclined angle exceeds a certain bound. The 3R-PRBM was proposed to overcome this weakness, consisting of three revolute joints, each accompanied by a torsion spring [37–39]. To reduce the complexity and computation time of the 3R-PRBM while increasing the accuracy of the 1R-PRBM, the 2R-PRBM emerged in [40]. To more accurately predict the behavior of compliant beams, the 5R-PRBM and Chained PRBM (CPRBM) have been proposed in recent years [41, 42]. Although PRBM is well-applied in designing various mechanisms [43–45], there are still some weaknesses in this modeling method, including unable to obtain accurate deformation shapes, simplified dynamics, and limited accuracy.

An alternative modeling approach, the Beam Constraint Model (BCM), provides closed-form solutions for fixed guided beams. The innovation of BCM lies in its capacity to depict the relationships between comprehensive loads and end-displacements, covering both translational and rotational movements, across a wide range, all while maintaining simplicity and accuracy [32, 33]. The Timoshenko BCM (TBCM) expands this framework to account for shear effects, thereby improving prediction accuracy [46, 47]. Furthermore, another modeling technique, the Bi-BCM, involves dividing a fixed-guided beam into two distinct beam elements. The BCM is then independently employed for each beam element and subsequently combined to yield a closed-form load-deflection solution. In this approach, the tip loads are represented as functions of tip deflections. This method particularly excels in modeling compliant beams with a single fixed end, making it well-suited for the analysis of compliant bistable mechanisms [48–51]. In addition, accurately predicting the effects of significant axial forces presents a challenge for BCM. This challenge was addressed by increasing the order of the BCM [52]. Moreover, a General Lumped-compliance Beam Model (GLBM) was introduced to address modeling challenges posed by complex compliant mechanisms [53]. Moreover, the dynamic beam constraint model (DBCM) addresses nonlinearity in intermediate-deformation compliant mechanisms, aiding kinetostatic and large-amplitude vibration analyses effectively [54].

The BCM and its derivative models, as previously stated, are limited to small deflection assumption, making them unsuitable for modeling compliant mechanisms undergoing large deformation. To tackle this challenge, researchers developed various alternative methods. Chained BCM (CBCM) is proposed for modeling large deflections in both straight and curved compliant beams and mechanisms [55, 56]. It aims to provide a versatile method for efficiently addressing a wide range of large deflection problems in such systems [57–61]. Besides, chained spatial BCM (CSBCM) was proposed to address the challenge of modeling spatial deflections in compliant mechanisms [62, 63]. While the CBCM and CSBCM methods successfully address the issue of handling large deformations, they introduce increased complexity into the modeling process. This complexity arises from their approach of dividing the beam into multiple sub-beams and applying the BCM to each of these segments. As the number of sub-beams increases, the computational complexity escalates, and the calculation process starts resembling finite element analysis (FEA). Moreover, these methods are unable to provide specific deformation shapes for compliant beams.

The elliptic integral solution (EIS) is widely recognized for its accuracy in analyzing large deflections in thin beams within compliant mechanisms [34, 64, 65]. The comprehensive elliptic integral solution (CEIS) also extends the elliptic integral solutions to be suitable for any beam end angle [66]. Within the framework of the EIS method, inflection points consistently constitute a central topic of discussion. These points are characterized by changes in curvature sign on a smooth plane curve, shifting between concave and convex shapes. The number of inflection points plays a pivotal role in the modeling process. Consequently, it becomes imperative to engage in discussions tailored to specific circumstances during the modeling endeavor. This causes an increase in the complexity of the modeling process while simultaneously reducing its universality.

The advent of the smooth curvature model (SCM) has brought the modeling complexity to a lower level, which efficiently describes compliant beams by approximating beam curvature with low-order polynomials.[30]. The smooth curvature model and its derived models aim to address the inherent limitations of the previously mentioned methods, which include their restricted applicability to small deformations, complex modeling requirements, lack of consideration for deformation shape, the necessity of inflection point analysis, and suitability only for straight beams.The Multiple SCM (MSCM), an extension of the fundamental SCM which split compliant structure into multiple beam elements and apply SCM to each of the beam element. This method is proficient in modeling intricate, highly compliant mechanisms [67]. Pongsiri et al. integrated the SCM with Lagrange multiplier and Newton-Raphson methods and applied Castigliano's principle of minimum strain-energy, resulting in a novel approach to address the grasp stability problem [68]. This energy method is based on SCM and now referred to as the 2nd-order SCME method.

In addition to the Newtonian methods discussed above, previous studies have established the groundwork for utilizing energy-based methodologies for the kinetostatic analysis of compliant mechanisms. A previous work has proposed an energy-based method utilizing three commonly used models (BCM, PRBM, and linear Euler-Bernoulli beam model) towards a generalized framework for kinetostatic analysis of planar compliant mechanisms [69]. Besides, another model integrates the screw theory with the energy method for accurate and efficient kinetostatic analysis of general compliant mechanisms [70]. As mentioned earlier in [42], a method combining the energy approach and Chained Pseudo-Rigid-Body Model (CPRBM) is proposed to address the nonlinear contact problem in contact-aided compliant mechanisms. In [71], an energy-based framework is proposed, in which both strain energy and complementary strain energy are integrated into the nonlinear kinetostatic modeling of compliant mechanisms passively. Within this framework, the strain energy and complementary strain energy are expressed using the BCM and integrated through two nonlinear energy theorems, namely Castigliano's first theorem and the Crotti–Engesser theorem.

The aforementioned 2nd-order SCME method has limitations in modeling the post-buckling behavior of compliant beams. To address this, we have enhanced the SCME method in this study by elevating it from 2nd-order to higher order (5th-order), enabling it to model more intricate buckling behaviors and provide an accurate kinetostatic model for compliant mechanisms. The high-order SCME method inherits all the advantages of the conventional 2nd-order SCME approach [68]. These advantages encompass the accurate prediction of various aspects, such as bending strain energy, deformation shape, reaction forces, and stress. Moreover, it is versatile in its applicability, allowing for the modeling of both straight and curved beams under large deformation while capturing complex buckling behavior. A comparative analysis is conducted to clarify the strengths of each modeling method, which are summarized in Table 1.

The SCME method enhances the energy-based modeling approach by employing a high-order smooth curvature model to mathematically model the large deformations in compliant bistable mechanisms. A notable advantage of SCME lies in its capacity to model beam curvature, deformation shapes, stress and bending strain energy using fewer variables, thus resulting in higher efficiency. Additionally, within this method, complex nonlinear behaviors are reformulated into solvable mathematical problems through optimization techniques. The objective of this optimization is to minimize the strain energy of the compliant beam, ensuring that its beam tip aligns with specified trajectory points. Therefore, this optimization approach achieves the nonlinear kinetostatic modeling capability for compliant beams. The decision to select bistable mechanisms as a case study, instead of other mechanisms, is grounded in their inherent strong nonlinear behaviors during the deformation process, enabling an assessment of the accuracy and efficiency of our model in addressing such strong nonlinear post-buckling behaviors. The proposed SCME method is applicable not only to bistable mechanisms but also to various other types of compliant mechanisms. Its potential applications extend to modeling initially-curved compliant beams, contact-aid design problems, and distributed load problems.

The novelties of this work can be summarized as follows:

(1) **Accurate and comprehensive modeling capability**: This study employs the high-order SCME method for modeling compliant bistable mechanisms, yielding direct accurate results for all performance characteristics including deformation shapes, forces, strain energy, and stress. Furthermore, these results have been validated through FEA simulations and experimental tests.

(2) **Efficient modeling**: Benefiting from the continuous smooth curvature model (without discretization), deriving bending strain energy, along with offering an explicit expression of the gradient of Lagrange function during the

Table 1: Comparative analysis of kinetostatic modeling methods for compliant mechanisms. Note: high-order SCME method is the method proposed in this work and highlighted in red. ”Large deformation buckling” refers to the capability of modeling compliant bistable mechanisms as they encounter large deformations, including the analysis of buckling beam.

	Modeling Method	Output			Beam type			Large-deformation buckling
		Deformation shape	Strain Energy	Stress	Straight	Curved	Generic with rigid body	
PRBM	PRBM [31]				✓			
	2R-PRBM [40]		✓		✓			
	3R-PRBM [37–39]	✓	✓		✓			
	5R-PRBM [41]	✓	✓		✓	✓		
	CPRBM [42]	✓	✓		✓	✓		✓
BCM	BCM [32, 33]		✓		✓			
	TBCM [46, 47]		✓		✓			
	3rd-order BCM [52]		✓		✓			
	GLMB [53]		✓		✓		✓	
	DBCM [54]		✓		✓			
	CBCM [55, 56]	✓	✓	✓	✓	✓		✓
	CSBCM [62, 63]	✓	✓	✓	✓	✓		✓
EIS	EIS [34, 64, 65]	✓	✓	✓	✓	✓		✓
	CEIS [66]	✓	✓	✓	✓	✓		✓
SCM	SCM [30]	✓	✓		✓	✓		
	MSCM [67]	✓	✓		✓	✓		
	SCME [68]	✓	✓	✓	✓	✓		
	High-order SCME	✓	✓	✓	✓	✓		✓

root-finding process, the SCME method enables quick/efficient modeling. This approach is comprehensively compared with FEA simulations, CBCM, and CPRBM. The comparison results prove that the modeling speed is much quicker without compromising modeling accuracy.

(3) **Applicability in full angle range**: The high-order SCME method (5th order) is capable of modeling compliant bistable mechanisms with varying inclined angles from 0 to 90 degrees without the need for discretization. This feature simplifies the process of modeling the compliant beams.

This paper is organized as follows: Section 2 introduces the details and principles of the SCME method. Section 3 applies the 5th-order SCME method to model compliant bistable mechanisms. The modeling results are verified by FEA simulations and experiment tests in section 4. Section 5 delivers a comprehensive discussion of the proposed method. Conclusions are finally drawn in Section 6.

2. SCME method

Castigliano’s principle of minimum strain energy indicates that for a structure subjected to external loads and constraints, the equilibrium configuration is achieved when the total strain energy in the structure is minimized [72]. As a fundamental concept in static analysis, the minimum strain energy is normally used to analyze and design various structures such as beams, trusses, frames, and shells. By minimizing the strain energy, the distribution of stress and deformation shape within these structures under different loading conditions can be determined.

The fundamental concept underlying the SCME method pertains to the determination of the equilibrium configuration of a compliant beam when its end is constrained to assume specific poses. These poses indicate the specific location and inclined angle of the beam tip. This problem is mathematically cast in the framework of the Lagrange function, wherein the objective is to minimize the bending strain energy, denoted as U_{b}, while maintaining conformity between the derived beam’s tip poses and the specified poses. The SCM method establishes a crucial link between the strain energy and the end-point position and orientation by introducing generalized coefficients, represented as $\boldsymbol{\alpha}$. The root-finding procedure is realized through the implementation of the Newton-Raphson method, a numerical iterative technique employed to approximate the roots. The modeling processes mentioned earlier can all be conducted in MATLAB.

2.1. Deriving bending strain energy with SCM

The SCM is an accurate, low-dimensional model of large deformation bending which is capable of precisely describe the configuration of compliant beams. This model is derived from the assumption that the beam in bending is smooth and therefore can be approximated by low-dimension polynomials. The constitutive assumption in the large-deformation Bernoulli model posits that the equilibrium rate of rotation along the beam's midline or neutral axis, should be equivalent to the local bending moment divided by the beam stiffness EI. The point s is positioned on the neutral line, where s ranges within the interval $[0, L]$. Based on the coordinate system established in Fig. 1, the curvature function of point s on the compliant beam is defined in Eq. (1):

$$\omega(\boldsymbol{\alpha}, s) = \omega_0(\boldsymbol{\kappa}, s) + \frac{M_{\mathrm{t}} + F_{\mathrm{y}}(x_{\mathrm{tip}} - x_{\mathrm{s}}) - F_{\mathrm{x}}(y_{\mathrm{tip}} - y_{\mathrm{s}})}{EI}, \tag{1}$$

where, $\omega(\boldsymbol{\alpha}, s)$ and $\omega(\boldsymbol{\kappa}, s)$ represent the curvature of point s on the deformed and initial undeformed beam, respectively. M_{t} is the applied moment at the tip of the beam, F_{x} and F_{y} are applied forces at the tip of the beam. The x_{s} and y_{s} are the coordinates of point s in coordinate system $\mathrm{O}_i\mathrm{X}_i\mathrm{Y}_i$, x_{tip} and y_{tip} are the coordinates of beam tip, ϕ_{s} and ϕ_{tip} represents the deflection angles with regard to X_i axis for point s and beam tip, respectively. E is the Young's modulus of material, I is the second moment of area. The generalized coordinates $\boldsymbol{\alpha}$ and $\boldsymbol{\kappa}$ will be specifically explained in the subsequent content of this section. The defined terminology can be seen in Fig. 1.

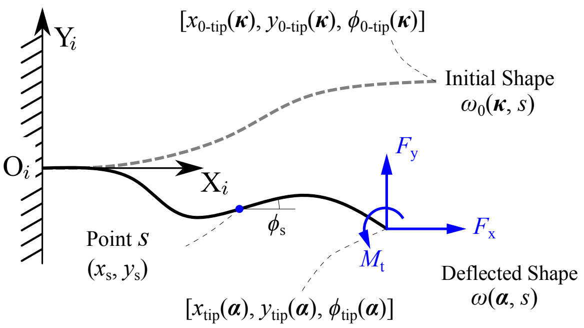

Figure 1: Terminologies employed in the explanation of the smooth curvature model. Initial shape of the beam represented by a gray dashed line. Deflected shape of the beam represented by a black continuous line. Beam root fixed to the ground. Formulation of curvature function before and after deflection using $\omega(\boldsymbol{\kappa}, s)$ and $\omega(\boldsymbol{\alpha}, s)$. Beam tip position before deflection: $[x_{0-\mathrm{tip}}(\boldsymbol{\kappa}), y_{0-\mathrm{tip}}(\boldsymbol{\kappa}), \phi_{0-\mathrm{tip}}(\boldsymbol{\kappa})]$. Tip position of the deflected beam after applying tip load F_{x}, F_{y}, and M_{t}: $[x_{\mathrm{tip}}(\boldsymbol{\alpha}), y_{\mathrm{tip}}(\boldsymbol{\alpha}), \phi_{\mathrm{tip}}(\boldsymbol{\alpha})]$ at equilibrium configuration. Coordinates of point s: $[x_{\mathrm{s}}, y_{\mathrm{s}}]$. Deflection angle at point s: ϕ_{s}.

Legendre polynomials have been applied in the form of summation to approximate the curvature of compliant beams. Legendre polynomials involve solving differential equations and representing functions as series expansions. The standard interval for Legendre polynomials is [-1, 1]. However, given the variation in the position of point $s = [0, L]$ along the beam. Therefore, the shifted Legendre polynomials within the interval [0, 1] is used for the approximation instead of using the standard Legendre polynomials within the interval [-1, 1][73]. The approximated curvature of deflected beam is expressed in Eq. (2):

$$\omega(\boldsymbol{\alpha}, s) \quad \approx \quad \frac{1}{L}\sum_{n=0}^{n=N} \alpha_n \psi_n(s), \tag{2}$$

where $\boldsymbol{\alpha} = (\alpha_0, \alpha_1, \cdots, \alpha_{\mathrm{N}})^T$ is a vector that contains the generalized coefficients. $\psi_n(s)$ represent the shifted Legendre polynomials. N is the order of shifted Legendre polynomials. The expression of shifted Legendre polynomials and its integration can be obtained from Tab. A.1 and Tab. A.2 in Appendix A. The mathematical expression for the curvature of an initially curved beam can be formulated as in Eq. (3):

$$\omega_0(\boldsymbol{\kappa}, s) \quad \approx \quad \frac{1}{L}\sum_{n=0}^{n=N} \kappa_n \psi_n(s), \tag{3}$$

where, $\boldsymbol{\kappa} = (\kappa_0, \kappa_1, \ldots, \kappa_{\mathrm{N}})^T$ represents a vector defined at the initial stage to characterize the compliant beam's initial shape prior to deflection. Consequently, $\boldsymbol{\kappa}$ constitutes a set of constant coefficients embedded within the nonlinear system. The beam tip coordinates at the undeformed configuration can be represented by $\left[x_{0-\mathrm{tip}}(\boldsymbol{\kappa}), y_{0-\mathrm{tip}}(\boldsymbol{\kappa}), \phi_{0-\mathrm{tip}}(\boldsymbol{\kappa})\right]$. In the case of the beam being initially straight, the curvature of its initial shape consistently remains zero, resulting in all $\kappa_n = 0$.

The variational formulation of the Euler-Bernoulli equations provides a direct approach to derive the bending strain energy by considering both the deflected beam curvature and the initial beam curvature. The expression for the bending strain energy is formulated as in Eq. (4):

$$U_{\mathrm{b}} = \frac{1}{2}\int_0^L EI\left(\omega(\alpha, s) - \omega_0(\kappa, s)\right)^2 ds. \tag{4}$$

The expression for the strain energy as a function of the generalized coefficients $\boldsymbol{\alpha}$ has been derived. It is imperative to establish a correlation between the coefficients $\boldsymbol{\alpha}$ and the beam tip position.

2.2. *Deriving beam tip position and orientation*

Curvature serves as a measure of the variation in the deflection angle along the longitudinal extent of the compliant beam. The deflection angle at a specific position s along the beam can be determined through the integration of beam curvature in Eq. (2). The expression of deflection angle can be obtained in Eq. (5):

$$\phi(\boldsymbol{\alpha}, s) = \int_0^s \omega(\boldsymbol{\alpha}, s) ds. \tag{5}$$

Determining the precise position and orientation of point s in the deflected compliant beam can precisely describe the deformation shape of compliant beam. The deflection angle at the tip of the beam can be derived when $s = L$. Except for α_0, other generalized coefficients are eliminated during integration. Hence, the tip angle ϕ_{tip} is mathematically equal to α_0. Tip position $[x_{\mathrm{tip}}, y_{\mathrm{tip}}]$ can be derived using trigonometrical relationship and integration from $s = 0$ to $s = L$. The expression of tip position and orientation can be obtained from Eq.(6), Eq.(7) and Eq.(8) :

$$\phi_{\mathrm{tip}}(\boldsymbol{\alpha}) \quad = \quad \phi(\boldsymbol{\alpha}, L) = \alpha_0, \tag{6}$$

$$x_{\mathrm{tip}}(\boldsymbol{\alpha}) \quad = \quad \int_0^L \cos\left(\phi(\boldsymbol{\alpha}, s)\right) ds, \tag{7}$$

$$y_{\mathrm{tip}}(\boldsymbol{\alpha}) \quad = \quad \int_0^L \sin\left(\phi(\boldsymbol{\alpha}, s)\right) ds. \tag{8}$$

Equations (7) and (8) are transcendental functions which cannot be expressed as solutions to polynomial equations with a finite number of terms. Alternatively, the integration process is carried out using a numerical method known as Gauss-Legendre quadrature. Gauss-Legendre quadrature is a method for approximating the definite integral of a function over a specified interval by computing a weighted sum of function values at a set of pre-determined sample points within that interval. To integrate deflection angles along the compliant beam, the Gauss-Legendre method involves using a set of five sample points to approximate the integral with high accuracy. The detail of Gauss-Legendre quadrature is explained in Appendix B. The derived expression of tip positions are list in Eq. (9) and Eq. (10):

$$x_{\mathrm{tip}}(\boldsymbol{\alpha}) \approx \frac{L}{2}\sum_{i=1}^{i=10} W_i \cos\left[\phi\left(\boldsymbol{\alpha}, \left(\frac{L}{2}x_i + \frac{L}{2}\right)\right)\right], \tag{9}$$

$$y_{\mathrm{tip}}(\boldsymbol{\alpha}) \approx \frac{L}{2}\sum_{i=1}^{i=10} W_i \sin\left[\phi\left(\boldsymbol{\alpha}, \left(\frac{L}{2}x_i + \frac{L}{2}\right)\right)\right], \tag{10}$$

where x_i represents the quadrature point, and W_i represents the weight. All x_i and W_i values are constant.

In this section, we have reached the stage of establishing the connection between the tip position, orientation of a compliant beam and the generalized coefficient vector $\boldsymbol{\alpha}$. As outlined in Eq. (4), we have also derived the expression for bending strain energy with regard to $\boldsymbol{\alpha}$. With this groundwork in place, we can now proceed to construct a Lagrangian function to address the optimization problem at hand. This problem entails determining the minimum magnitude of bending strain energy while ensuring that the beam tip position and orientation align with a specific target configuration.

2.3. *Constructing Lagrangian function and nonlinear equation system*

The Lagrange multipliers approach is a technique employed to identify the local maximum and minimum points of a function while taking into account equation constraints [74]. The solution of Lagrangian function must satisfy these equation constraints. The expression of Lagrange function can be obtained from Eq. (11):

$$\mathcal{L}(\boldsymbol{x}, \boldsymbol{\lambda}) = f(\boldsymbol{x}) + \boldsymbol{\lambda} \cdot \boldsymbol{g}(\boldsymbol{x}), \tag{11}$$

where the $f(\boldsymbol{x})$ is the objective function while the $g(\boldsymbol{x})$ is the constraint function. The variables need to be solved are $\boldsymbol{x}$ and $\boldsymbol{\lambda}$. This function can be explained from an alternative expression: find the maximum or minimum of objective function $f(\boldsymbol{x})$ when $g(\boldsymbol{x}) = 0$. In the bending strain energy minimization process, we construct the Lagrangian function as in Eq. (12):

$$\mathcal{L}(\boldsymbol{\alpha}, \boldsymbol{\lambda}) = U_{\mathrm{b}}(\boldsymbol{\alpha}) + \begin{bmatrix}\lambda_1 & \lambda_2 & \lambda_3\end{bmatrix}\begin{bmatrix} x_{\mathrm{g}} - x_{\mathrm{tip}}(\boldsymbol{\alpha}) \\ y_{\mathrm{g}} - y_{\mathrm{tip}}(\boldsymbol{\alpha}) \\ \phi_{\mathrm{g}} - \phi_{\mathrm{tip}}(\boldsymbol{\alpha}) \end{bmatrix}. \tag{12}$$

The constraint equation specifies that the tip position and orientation of the compliant beam should be equal to the given tip position and orientation $[x_{\mathrm{g}}, y_{\mathrm{g}}, \phi_{\mathrm{g}}]^{\mathrm{T}}$. The formed Lagrangian can be understood as follows: finding the minimum strain energy of the compliant beam when the tip position and orientation is predetermined. When the objective function reaches its stationary point, indicating a local extreme value, the partial derivatives of each individual parameter are zero. Consequently, we can derive the nonlinear equation system as in Eq.(13):

$$\frac{\partial \mathcal{L}}{\partial \boldsymbol{\alpha}} = \frac{\partial \mathcal{L}}{\partial \boldsymbol{\lambda}} = 0. \tag{13}$$

This complex nonlinear equation system is challenging to solve. Therefore, it requires the application of a numerical method. In this work, Newton-Raphson method is selected to approximate the roots of the constructed nonlinear equation system.

2.4. *Deriving the deflected shape of compliant beams*

After obtaining the solution $\boldsymbol{\alpha}^*$ for the Lagrangian function, the next step is to derive the deformation shape of compliant beams. To visualize the deformation shape, one simple method is to determine the positions of each point

s along the beam, which is formulated in Eq. (14) and Eq. (15):

$$x(s) \approx \frac{s}{2}\sum_{i=1}^{i=10} W_i \cos\left[\phi\left(\boldsymbol{\alpha}^*, \left(\frac{s}{2}x_i + \frac{s}{2}\right)\right)\right], \tag{14}$$

$$y(s) \approx \frac{s}{2}\sum_{i=1}^{i=10} W_i \sin\left[\phi\left(\boldsymbol{\alpha}^*, \left(\frac{s}{2}x_i + \frac{s}{2}\right)\right)\right]. \tag{15}$$

By selecting a finite number of discrete points along the beam, it becomes feasible to determine the coordinates of each individual point, thereby deriving the deformation shape of the beam. Furthermore, the ability to predict beam deformation shape plays a crucial role in modeling contact-aided compliant mechanisms.

3. Modeling compliant bistable mechanism

Modeling of compliant bistable mechanisms under large deformation is particularly challenging due to its significant geometric nonlinearity after the buckling occurs. To avoid snap-through behavior in bistable mechanisms, modeling and simulation are always controlled by providing a specific trajectory, thereby deriving the corresponding applied force, i.e., displacement-driven modeling. This section would demonstrate the details of modeling the compliant bistable mechanisms using 5th-order SCME method.

In preparation for the modeling process, a series of fundamental considerations must be addressed. Firstly, it is essential to establish a well-defined coordinate system that will serve as the foundational reference frame for the following analysis. Subsequently, determining the trajectory of the beam tip is necessary to simulate the movement of the center shuttle. Following these preparations, the modeling of the compliant bistable mechanism is conducted. The following Fig. 2 illustrates the definition of local and global coordinate system and also the definition of trajectory points and geometric parameters.

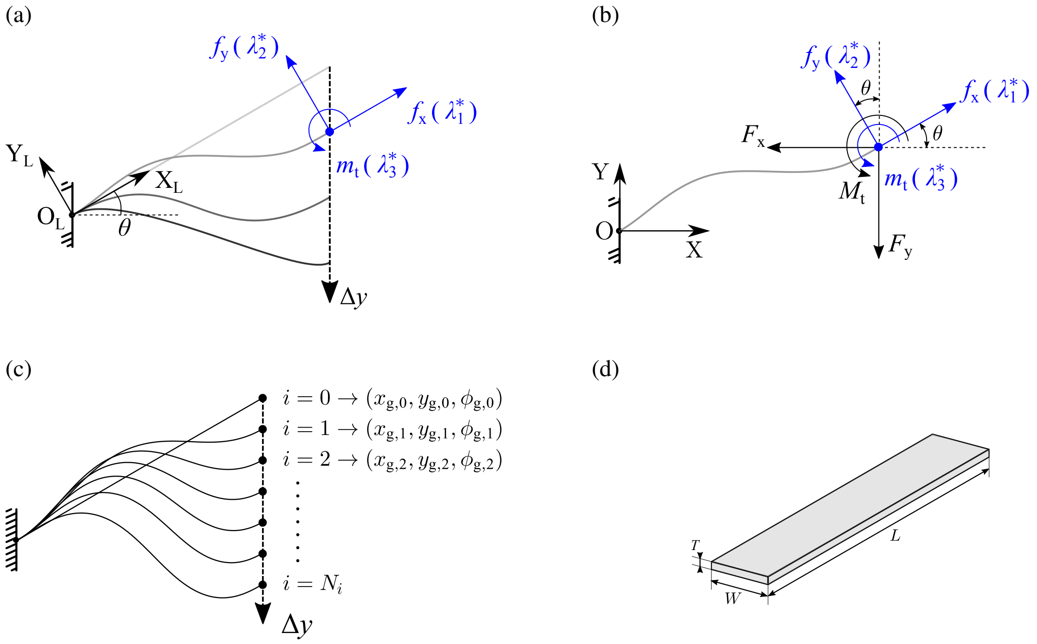

Figure 2: Explanation of local and global coordinate systems, trajectory points, and geometric parameters of compliant beams.(a) Definition of local coordinate system: X_L axis aligned with the beam's initial shape, while Y_L axis perpendicular to X_L axis. Origin, O_L, fixed at root of compliant beam. Initial inclined angle of compliant beam in global coordinate system denoted as θ, constant during modeling procedure. Forces f_x, f_y, and moment m_t, determined using the Lagrange multiplier method, defined in the local coordinate framework with positive direction marked as blue arrows. (b) Definition of global coordinate system: The global coordinate system, with origin O at the beam root, features horizontal X and vertical Y axes. Forces F_x, F_y, and moment M_t in global coordinate system composed from forces f_x, f_y, and moment m_t in local coordinate system. Positive directions of force and moment in the global system marked as black arrows. (c) Definition of discrete trajectory points: Overall displacement, Δy, with N_i points evenly distributed on the trajectory. The coordinates of i-th trajectory point is $[x_{g,i}, y_{g,i}]$ with deflected angle $\phi_{g,i}$. (d) Definition of geometric parameters: The beam length denoted as L; the in-plane thickness denoted as T; the out-of-plane thickness denoted as W.

Following the establishment of both material and geometric properties, the subsequent step involves determining the trajectory of the beam tip. The tip trajectory is defined to move along the negative direction of the Y-axis in the global coordinate system, as shown in Fig. 2 (c). The straight trajectory is discretized into finite trajectory points, and the amount of these points is denoted as N_i. The index of these discrete points is denoted as i. The coordinates of each trajectory point in local coordinate system $O_L X_L Y_L$ can be calculated using Eq. (16), Eq. (17) and Eq. (18).

$$x_{g,i} = L - i\frac{\Delta y \sin\theta}{N_i}, \tag{16}$$

$$y_{g,i} = -i\frac{\Delta y \cos\theta}{N_i}, \tag{17}$$

$$\phi_{g,i} = \theta, \tag{18}$$

where, $[x_{g,i}, y_{g,i}, \phi_{g,i}]$ represents the coordinates of i-th given tip poses in the trajectory. Δy is the hypothetical length of trajectory. The inclined angle θ of the compliant beam is initially defined and remains constant in this formulation. In Fig. 2 (d), W, T and L represent the out-of-plane thickness, in-plane thickness, and length of the compliant beam, respectively.

Typically, a 2nd-order polynomial, which was previously utilized in modeling compliant grippers, can effectively simulate a beam with two inflection points [68]. However, when dealing with the modeling of compliant bistable mechanisms, employing a lower-order polynomial is no longer suitable due to the intricate deformation exhibited by buckled compliant beams. These deformation shapes typically involve more inflection points.

As the compliant beam to be modeled possesses an initial straight configuration, the curvature of the initial state remains consistently zero, denoted as $\omega_0(\boldsymbol{\kappa}, s) = 0$. Consequently, this condition implies that all the terms in generalized coordinate vector $\boldsymbol{\kappa}$ are equal to zero. The expression for the fitted curvature function can be formulated as in Eq. (19):

$$\begin{aligned}
\omega(\boldsymbol{\alpha}, s) \;=\;& \frac{\alpha_0}{L} + \frac{\alpha_1}{L}\left(\frac{2s}{L} - 1\right) + \frac{\alpha_2}{L}\left(\frac{6s^2}{L^2} - \frac{6s}{L} + 1\right) \\
&+ \frac{\alpha_3}{L}\left(\frac{20s^3}{L^3} - \frac{30s^2}{L^2} + \frac{12s}{L} - 1\right) + \frac{\alpha_4}{L}\left(\frac{70s^4}{L^4} - \frac{140s^3}{L^3} + \frac{90s^2}{L^2} - \frac{20s}{L} + 1\right) \\
&+ \frac{\alpha_5}{L}\left(\frac{252s^5}{L^5} - \frac{630s^4}{L^4} + \frac{560s^3}{L^3} - \frac{210s^2}{L^2} + \frac{30s}{L} - 1\right). \qquad (19)
\end{aligned}$$

Thereby we can obtain the orientation of point s by integrating beam curvature $\omega(\boldsymbol{\alpha}, s)$ as in Eq. (20):

$$\begin{aligned}
\phi(\boldsymbol{\alpha}, s) \;=\;& \alpha_0\frac{s}{L} + \alpha_1\left(\frac{s^2}{L^2} - \frac{s}{L}\right) + \alpha_2\left(\frac{2s^3}{L^3} - \frac{3s^2}{L^2} + \frac{s}{L}\right) \\
&+ \alpha_3\left(\frac{5s^4}{L^4} - \frac{10s^3}{L^3} + \frac{6s^2}{L^2} - \frac{s}{L}\right) + \alpha_4\left(\frac{14s^5}{L^5} - \frac{35s^4}{L^4} + \frac{30s^3}{L^3} - \frac{10s^2}{L^2} + \frac{s}{L}\right) \\
&+ \alpha_5\left(\frac{42s^6}{L^6} - \frac{126s^5}{L^5} + \frac{140s^4}{L^4} - \frac{70s^3}{L^3} + \frac{15s^2}{L^2} - \frac{s}{L}\right). \qquad (20)
\end{aligned}$$

Subsequently, the beam's tip position and orientation can be determined through substitute Eq. (20) into Eq. (7) and (8). The derived expression of tip position and orientation, values of weights, denoted as W_i, and the quadrature points, represented as x_i, can be found in Appendix B. Given that both the weights and quadrature points maintain a constant magnitude, it is noteworthy that the tip position and orientation are inherently corresponds solely with the generalized coordinates $\boldsymbol{\alpha}$. Thereby, integrate the beam curvature and we can obtain the expression of bending strain energy as in Eq. (21):

$$U_\mathrm{b}(\boldsymbol{\alpha}) = \frac{EI}{2L}\left(\alpha_0^2 + \frac{\alpha_1^2}{3} + \frac{\alpha_2^2}{5} + \frac{\alpha_3^2}{7} + \frac{\alpha_4^2}{9} + \frac{\alpha_5^2}{11}\right). \qquad (21)$$

At this stage, having formulated all the basic equations, we need to conduct the second partial derivative test [75]. This technique in multivariable calculus helps determine whether a critical point of a function is a local minimum, maximum, or a saddle point. If the Hessian matrix (the matrix of second-order partial derivatives) is positive definite at the stationary point, it signifies a minimum. This is confirmed when all eigenvalues of the Hessian matrix are positive, indicating that the function curves upwards in all directions around that critical point. The Hessian matrix of the Lagrangian function with regard to $\boldsymbol{\alpha}$ can be obtained in Eq. (22):

$$\frac{\partial^2 U_\mathrm{b}}{\partial(\alpha_i)^2} = \begin{bmatrix} \frac{\partial^2 U_\mathrm{b}}{\partial(\alpha_0)^2} & \frac{\partial^2 U_\mathrm{b}}{\partial\alpha_0\partial\alpha_1} & \cdots & \frac{\partial^2 U_\mathrm{b}}{\partial\alpha_0\partial\alpha_5} \\ \frac{\partial^2 U_\mathrm{b}}{\partial\alpha_1\partial\alpha_0} & \frac{\partial^2 U_\mathrm{b}}{\partial\alpha_1^2} & \cdots & \frac{\partial^2 U_\mathrm{b}}{\partial\alpha_1\partial\alpha_5} \\ \vdots & \vdots & \ddots & \vdots \\ \frac{\partial^2 U_\mathrm{b}}{\partial\alpha_5\partial\alpha_0} & \frac{\partial^2 U_\mathrm{b}}{\partial\alpha_5\partial\alpha_1} & \cdots & \frac{\partial^2 U_\mathrm{b}}{\partial\alpha_5^2} \end{bmatrix} = \begin{bmatrix} \frac{EI}{L} & 0 & 0 & 0 & 0 & 0 \\ 0 & \frac{EI}{3L} & 0 & 0 & 0 & 0 \\ 0 & 0 & \frac{EI}{5L} & 0 & 0 & 0 \\ 0 & 0 & 0 & \frac{EI}{7L} & 0 & 0 \\ 0 & 0 & 0 & 0 & \frac{EI}{9L} & 0 \\ 0 & 0 & 0 & 0 & 0 & \frac{EI}{11L} \end{bmatrix}. \qquad (22)$$

In the resulting diagonal matrix, all eigenvalues are positive constantly. Consequently, it is straightforward to proves that the stationary point obtained from Lagrange multiplier method is corresponding to the minimum strain energy. Accordingly, the Lagrangian function in Eq. (12) can be reformulated as in Eq. (23):

$$\mathcal{L}(\boldsymbol{\alpha},\boldsymbol{\lambda}) = \frac{EI}{2L}\left(\alpha_0^2 + \frac{\alpha_1^2}{3} + \frac{\alpha_2^2}{5} + \frac{\alpha_3^2}{7} + \frac{\alpha_4^2}{9} + \frac{\alpha_5^2}{11}\right) + \begin{bmatrix}\lambda_1 & \lambda_2 & \lambda_3\end{bmatrix}\begin{bmatrix} x_{\mathrm{g},i} - x_{\mathrm{tip}}(\boldsymbol{\alpha}) \\ y_{\mathrm{g},i} - y_{\mathrm{tip}}(\boldsymbol{\alpha}) \\ \phi_{\mathrm{g},i} - \phi_{\mathrm{tip}}(\boldsymbol{\alpha}) \end{bmatrix}. \tag{23}$$

The strain energy reach its local minimum when the Lagrangian function reaches its stationary point. At that point, all the partial derivative of Lagrangian function is equal to zero which result in a nonlinear system with eight equations. The derived nonlinear equation system is expressed in Eq. (24):

$$\begin{cases}
\dfrac{\partial\mathcal{L}}{\partial\alpha_0} = \dfrac{EI}{L}\alpha_0 - \lambda_1\dfrac{\partial x_{\mathrm{tip}}(\boldsymbol{\alpha})}{\partial\alpha_0} - \lambda_2\dfrac{\partial y_{\mathrm{tip}}(\boldsymbol{\alpha})}{\partial\alpha_0} - \lambda_3\dfrac{\partial \phi_{\mathrm{tip}}(\boldsymbol{\alpha})}{\partial\alpha_0} & = 0, \\
\dfrac{\partial\mathcal{L}}{\partial\alpha_1} = \dfrac{EI}{3L}\alpha_1 - \lambda_1\dfrac{\partial x_{\mathrm{tip}}(\boldsymbol{\alpha})}{\partial\alpha_1} - \lambda_2\dfrac{\partial y_{\mathrm{tip}}(\boldsymbol{\alpha})}{\partial\alpha_1} - \lambda_3\dfrac{\partial \phi_{\mathrm{tip}}(\boldsymbol{\alpha})}{\partial\alpha_1} & = 0, \\
\dfrac{\partial\mathcal{L}}{\partial\alpha_2} = \dfrac{EI}{5L}\alpha_2 - \lambda_1\dfrac{\partial x_{\mathrm{tip}}(\boldsymbol{\alpha})}{\partial\alpha_2} - \lambda_2\dfrac{\partial y_{\mathrm{tip}}(\boldsymbol{\alpha})}{\partial\alpha_2} - \lambda_3\dfrac{\partial \phi_{\mathrm{tip}}(\boldsymbol{\alpha})}{\partial\alpha_2} & = 0, \\
\dfrac{\partial\mathcal{L}}{\partial\alpha_3} = \dfrac{EI}{7L}\alpha_3 - \lambda_1\dfrac{\partial x_{\mathrm{tip}}(\boldsymbol{\alpha})}{\partial\alpha_3} - \lambda_2\dfrac{\partial y_{\mathrm{tip}}(\boldsymbol{\alpha})}{\partial\alpha_3} - \lambda_3\dfrac{\partial \phi_{\mathrm{tip}}(\boldsymbol{\alpha})}{\partial\alpha_3} & = 0, \\
\dfrac{\partial\mathcal{L}}{\partial\alpha_4} = \dfrac{EI}{9L}\alpha_4 - \lambda_1\dfrac{\partial x_{\mathrm{tip}}(\boldsymbol{\alpha})}{\partial\alpha_4} - \lambda_2\dfrac{\partial y_{\mathrm{tip}}(\boldsymbol{\alpha})}{\partial\alpha_4} - \lambda_3\dfrac{\partial \phi_{\mathrm{tip}}(\boldsymbol{\alpha})}{\partial\alpha_4} & = 0, \\
\dfrac{\partial\mathcal{L}}{\partial\alpha_5} = \dfrac{EI}{11L}\alpha_5 - \lambda_1\dfrac{\partial x_{\mathrm{tip}}(\boldsymbol{\alpha})}{\partial\alpha_5} - \lambda_2\dfrac{\partial y_{\mathrm{tip}}(\boldsymbol{\alpha})}{\partial\alpha_5} - \lambda_3\dfrac{\partial \phi_{\mathrm{tip}}(\boldsymbol{\alpha})}{\partial\alpha_5} & = 0, \\
\dfrac{\partial\mathcal{L}}{\partial\lambda_1} = x_{\mathrm{g},i} - x_{\mathrm{tip}}(\boldsymbol{\alpha}) = 0, \\
\dfrac{\partial\mathcal{L}}{\partial\lambda_2} = y_{\mathrm{g},i} - y_{\mathrm{tip}}(\boldsymbol{\alpha}) = 0, \\
\dfrac{\partial\mathcal{L}}{\partial\lambda_3} = \phi_{\mathrm{g},i} - \phi_{\mathrm{tip}}(\boldsymbol{\alpha}) = 0.
\end{cases} \tag{24}$$

Utilizing numerical iteration, specifically the Newton-Raphson method, enables the determination of the stationary point of the Lagrangian function. Typically, Lagrangian multipliers assume distinct meanings when addressing optimization problems. In the context of modeling compliant beams, we assume that the Lagrange multipliers $\boldsymbol{\lambda}$ represent the applied force and moment at the tip. To verify this assumption, the proof procedure is demonstrated as:

a) Based on Eq. (24), the solution ($\boldsymbol{\alpha}^*$and $\boldsymbol{\lambda}^*$) to the Lagrangian function can be treated as a function of $x_{\mathrm{g},i}$, $y_{\mathrm{g},i}$, and $\phi_{\mathrm{g},i}$, denoted as $\boldsymbol{\alpha}^*(x_{\mathrm{g},i}, y_{\mathrm{g},i}, \phi_{\mathrm{g},i})$ and $\boldsymbol{\lambda}^*(x_{\mathrm{g},i}, y_{\mathrm{g},i}, \phi_{\mathrm{g},i})$. The obtained minimum bending strain energy which denoted as $U_{\mathrm{b}}(\boldsymbol{\alpha}^*)$ can be further reformulated as $U_{\mathrm{b}}\left[\boldsymbol{\alpha}^*(x_{\mathrm{g},i}, y_{\mathrm{g},i}, \phi_{\mathrm{g},i})\right]$. The expression of the Lagrange function at the stationary point is reformulated as in Eq. (25):

$$\mathcal{L}[\boldsymbol{\alpha}^*(x_{\mathrm{g},i}, y_{\mathrm{g},i}, \phi_{\mathrm{g},i}), \boldsymbol{\lambda}^*(x_{\mathrm{g},i}, y_{\mathrm{g},i}, \phi_{\mathrm{g},i}), x_{\mathrm{g},i}, y_{\mathrm{g},i}, \phi_{\mathrm{g},i}] = U_{\mathrm{b}}\left[\boldsymbol{\alpha}^*(x_{\mathrm{g},i}, y_{\mathrm{g},i}, \phi_{\mathrm{g},i})\right] = U_{\mathrm{b}}(x_{\mathrm{g},i}, y_{\mathrm{g},i}, \phi_{\mathrm{g},i}), \tag{25}$$

where, the constraint components are eliminated due to $g(x) = 0$ at stationary point.

b) Derive the partial derivative of $U_{\mathrm{b}}(x_{\mathrm{g},i}, y_{\mathrm{g},i}, \phi_{\mathrm{g},i})$ with regard to $x_{\mathrm{g},i}$, $y_{\mathrm{g},i}$, $\phi_{\mathrm{g},i}$ at the stationary point and based on the multivariable chain rule, we can obtain Eq. (26), (27) and (28):

$$\begin{aligned}
\frac{\partial U_{\mathrm{b}}(x_{\mathrm{g},i}, y_{\mathrm{g},i}, \phi_{\mathrm{g},i})}{\partial x_{\mathrm{g},i}} &= \frac{\partial\mathcal{L}[\boldsymbol{\alpha}^*(x_{\mathrm{g},i}, y_{\mathrm{g},i}, \phi_{\mathrm{g},i}), \boldsymbol{\lambda}^*(x_{\mathrm{g},i}, y_{\mathrm{g},i}, \phi_{\mathrm{g},i}), x_{\mathrm{g},i}, y_{\mathrm{g},i}, \phi_{\mathrm{g},i}]}{\partial x_{\mathrm{g},i}} \\
&= \cancel{\frac{\partial\mathcal{L}}{\partial\boldsymbol{\alpha}}}\frac{\partial\boldsymbol{\alpha}^*}{\partial x_{\mathrm{g},i}} + \cancel{\frac{\partial\mathcal{L}}{\partial\boldsymbol{\lambda}}}\frac{\partial\boldsymbol{\lambda}^*}{\partial x_{\mathrm{g},i}} + \frac{\partial\mathcal{L}}{\partial x_{\mathrm{g},i}}\frac{dx_{\mathrm{g},i}}{dx_{\mathrm{g},i}} + \frac{\partial\mathcal{L}}{\partial y_{\mathrm{g},i}}\cancel{\frac{dy_{\mathrm{g},i}}{dx_{\mathrm{g},i}}} + \frac{\partial\mathcal{L}}{\partial \phi_{\mathrm{g},i}}\cancel{\frac{d\phi_{\mathrm{g},i}}{dx_{\mathrm{g},i}}},
\end{aligned} \tag{26}$$

$$\begin{aligned}\frac{\partial U_{\mathrm{b}}(x_{\mathrm{g},i}, y_{\mathrm{g},i}, \phi_{\mathrm{g},i})}{\partial y_{\mathrm{g},i}} &= \frac{\partial \mathcal{L}[\boldsymbol{\alpha}^*(x_{\mathrm{g},i}, y_{\mathrm{g},i}, \phi_{\mathrm{g},i}), \boldsymbol{\lambda}^*(x_{\mathrm{g},i}, y_{\mathrm{g},i}, \phi_{\mathrm{g},i}), x_{\mathrm{g},i}, y_{\mathrm{g},i}, \phi_{\mathrm{g},i}]}{\partial y_{\mathrm{g},i}} \\ &= \cancel{\frac{\partial \mathcal{L}}{\partial \boldsymbol{\alpha}}} \frac{\partial \boldsymbol{\alpha}^*}{\partial y_{\mathrm{g},i}} + \cancel{\frac{\partial \mathcal{L}}{\partial \boldsymbol{\lambda}}} \frac{\partial \boldsymbol{\lambda}^*}{\partial y_{\mathrm{g},i}} + \frac{\partial \mathcal{L}}{\partial x_{\mathrm{g},i}} \cancel{\frac{d x_{\mathrm{g},i}}{d y_{\mathrm{g},i}}} + \frac{\partial \mathcal{L}}{\partial y_{\mathrm{g},i}} \frac{d y_{\mathrm{g},i}}{d y_{\mathrm{g},i}} + \frac{\partial \mathcal{L}}{\partial \phi_{\mathrm{g},i}} \cancel{\frac{d \phi_{\mathrm{g},i}}{d y_{\mathrm{g},i}}},\end{aligned} \tag{27}$$

$$\begin{aligned}\frac{\partial U_{\mathrm{b}}(x_{\mathrm{g},i}, y_{\mathrm{g},i}, \phi_{\mathrm{g},i})}{\partial \phi_{\mathrm{g},i}} &= \frac{\partial \mathcal{L}[\boldsymbol{\alpha}^*(x_{\mathrm{g},i}, y_{\mathrm{g},i}, \phi_{\mathrm{g},i}), \boldsymbol{\lambda}^*(x_{\mathrm{g},i}, y_{\mathrm{g},i}, \phi_{\mathrm{g},i}), x_{\mathrm{g},i}, y_{\mathrm{g},i}, \phi_{\mathrm{g},i}]}{\partial \phi_{\mathrm{g},i}} \\ &= \cancel{\frac{\partial \mathcal{L}}{\partial \boldsymbol{\alpha}}} \frac{\partial \boldsymbol{\alpha}^*}{\partial \phi_{\mathrm{g},i}} + \cancel{\frac{\partial \mathcal{L}}{\partial \boldsymbol{\lambda}}} \frac{\partial \boldsymbol{\lambda}^*}{\partial \phi_{\mathrm{g},i}} + \frac{\partial \mathcal{L}}{\partial x_{\mathrm{g},i}} \cancel{\frac{d x_{\mathrm{g},i}}{d \phi_{\mathrm{g},i}}} + \frac{\partial \mathcal{L}}{\partial y_{\mathrm{g},i}} \cancel{\frac{d y_{\mathrm{g},i}}{d \phi_{\mathrm{g},i}}} + \frac{\partial \mathcal{L}}{\partial \phi_{\mathrm{g},i}} \frac{d \phi_{\mathrm{g},i}}{d \phi_{\mathrm{g},i}}.\end{aligned} \tag{28}$$

c) At the stationary point, both $\partial\mathcal{L}/\partial\boldsymbol{\alpha}$ and $\partial\mathcal{L}/\partial\boldsymbol{\lambda}$ equal zero. Furthermore, the coordinates $x_{\mathrm{g},i}, y_{\mathrm{g},i}, \phi_{\mathrm{g},i}$ are mutually independent. Hence Eq. (26-28) can be simplified to:

$$\frac{\partial U_{\mathrm{b}}(x_{\mathrm{g},i}, y_{\mathrm{g},i}, \phi_{\mathrm{g},i})}{\partial x_{\mathrm{g},i}} = \frac{\partial \mathcal{L}}{\partial x_{\mathrm{g},i}} \frac{d x_{\mathrm{g},i}}{d x_{\mathrm{g},i}} = \lambda_1, \tag{29}$$

$$\frac{\partial U_{\mathrm{b}}(x_{\mathrm{g},i}, y_{\mathrm{g},i}, \phi_{\mathrm{g},i})}{\partial y_{\mathrm{g},i}} = \frac{\partial \mathcal{L}}{\partial y_{\mathrm{g},i}} \frac{d y_{\mathrm{g},i}}{d y_{\mathrm{g},i}} = \lambda_2, \tag{30}$$

$$\frac{\partial U_{\mathrm{b}}(x_{\mathrm{g},i}, y_{\mathrm{g},i}, \phi_{\mathrm{g},i})}{\partial \phi_{\phi,i}} = \frac{\partial \mathcal{L}}{\partial \phi_{\mathrm{g},i}} \frac{d \phi_{\mathrm{g},i}}{d \phi_{\mathrm{g},i}} = \lambda_3. \tag{31}$$

d) Castigliano's first theorem indicates that, the first partial derivative of the total internal energy (strain energy) in a structure with respect to any particular deflection component at a point is equal to the force applied at that point and in the direction corresponding to that deflection component. In our derivation process, the Lagrangian multipliers indeed represent the first partial derivative of the internal energy. Consequently, we can prove that the obtained Lagrange multipliers $\boldsymbol{\lambda}$ correspond to the applied forces and moment on the beam tip. Specifically, λ_1, λ_2 and λ_3 denote the applied forces f_{x}, f_{y} and moment m_{t} on the beam tip in the local coordinate system.

The aforementioned procedure is commonly referred to as the interpretation of Lagrange multipliers [76]. Eq. (32), Eq. (33) and Eq. (34) can be employed to transform the reaction force and moment from the local coordinate system to the global coordinate system as:

$$\begin{aligned} F_{\mathrm{x}} &= -f_{\mathrm{x}} \cos\theta + f_{\mathrm{y}} \sin\theta = -\lambda_1^* \cos\theta + \lambda_2^* \sin\theta, && (32)\\ F_{\mathrm{y}} &= -f_{\mathrm{x}} \sin\theta - f_{\mathrm{y}} \cos\theta = -\lambda_1^* \sin\theta - \lambda_2^* \cos\theta, && (33)\\ M_{\mathrm{t}} &= m_{\mathrm{t}} = \lambda_3^*. && (34)\end{aligned}$$

Determining the applied force on the beam tip is crucial for assessing stress in the modeling of compliant bistable mechanisms. This evaluation is essential to ensure the structural integrity, performance, and safety of these mechanisms. After determining the stationary point, the generalized coordinates are thereby determined, and the curvature of the beam can be easily obtained by substituting the $\boldsymbol{\alpha}^*$ into Eq. (19). In addition, the maximum bending stress, occurs at the extreme fiber of the beam, at point s can be calculated using SCME method by invoking Eq.(35):

$$\sigma_{\mathrm{b}}(s) = \frac{M}{I} \cdot \frac{T}{2} = \frac{EI\omega(s)}{I} \cdot \frac{T}{2} = \frac{ET\omega(s)}{2}, \tag{35}$$

where, $\sigma_{\mathrm{b}}(s)$ represent the bending stress at the extreme fiber of compliant beam at point s.

The Newton-Raphson method is an iterative numerical technique used to find the roots of a nonlinear equation [77, 78]. The Newton-Raphson method starts with an initial guess for the root of the equation and then iteratively refines this guess to approach the actual root. It is based on the idea of using the tangent line approximation to the function at the current guess to find a better approximation for the root. During the process of seeking the minimum bending strain energy, the primary objective is to determine the stationary point of the nonlinear equation system in Eq. (24). The root-finding algorithm can be seen from the flow chart in Fig. 3.

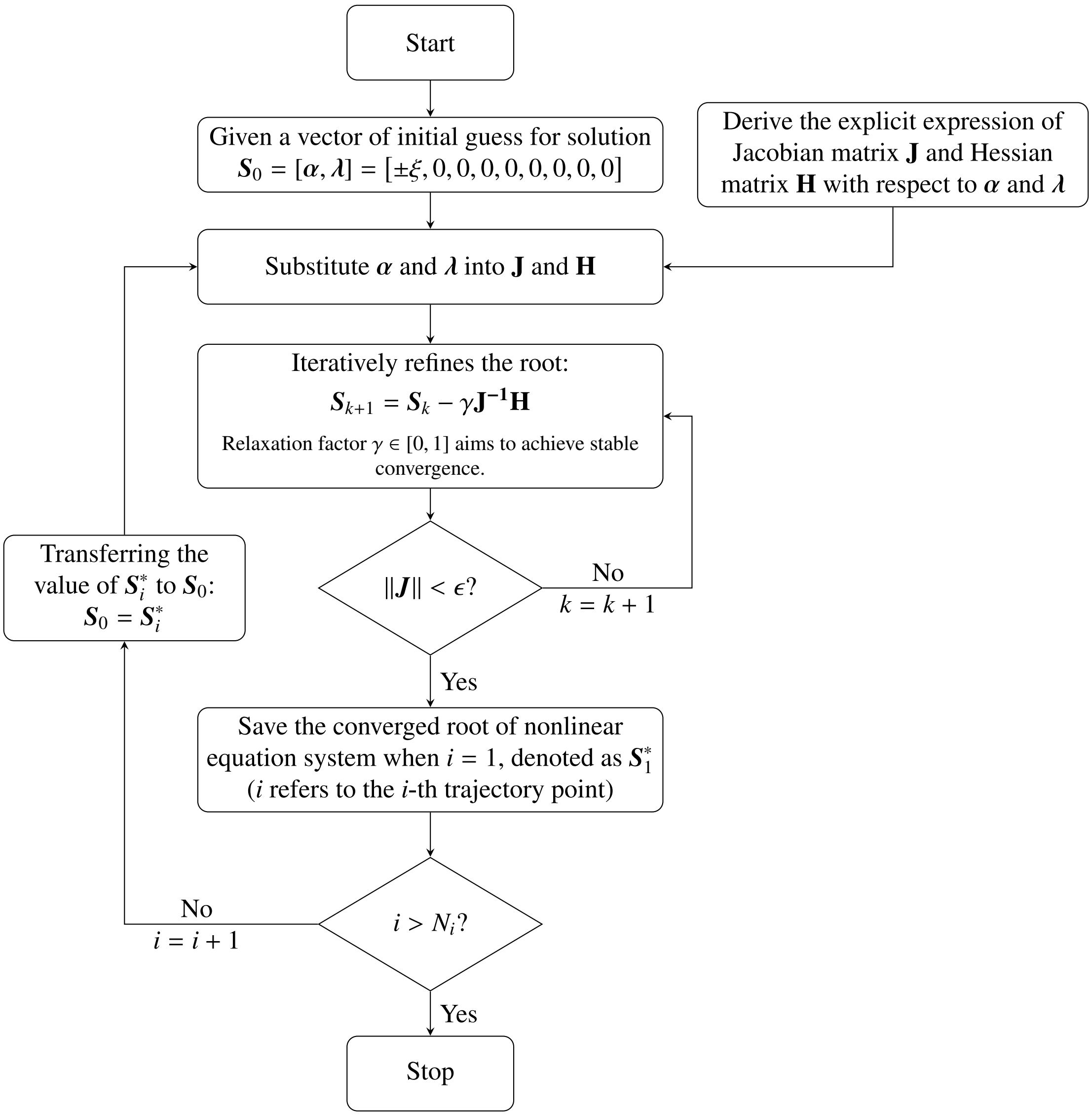

Figure 3: The flowchart of the root-finding algorithm. Before conducting the iteration, the explicit expressions of the Jacobian matrix **J** and Hessian matrices **H** need to be derived and used as part of the formulation during the iteration process. Then, the root-finding algorithm begins with a given initial guess S_0. The Newton-Raphson method is then applied to determine the root of the Lagrange function as demonstrated in the flowchart. The iteration stops when the norms of the gradients have converged to the threshold ϵ. Subsequently, the iteration process is applied to each trajectory point sequentially, until the last trajectory point.

When using the Newton-Raphson method, providing an initial guess of the root is vital, which influences the deformation shape as it determines the starting point for the iteration process. The iterative root-finding process relies on updating this initial guess. Notably, choosing an initial guess of zero can entirely lead to matrix singularity, making iteration difficult or impossible and obstructing convergence toward the root of the nonlinear equation system. The distinct deformation shapes, as shown in Fig. 4 (a) and (b), do not affect the mechanical characteristics of the mechanism. This problem can also be seen as a multi-solution problem, where a deformation shape corresponds to a valid solution.

In the proposed SCME method, the specified initial guess set as $S_0 = [\alpha, \lambda] = [\pm\xi, 0, 0, 0, 0, 0, 0, 0, 0]$ effectively meets the requirement of providing an initial guess used to be updated while ensuring that compliant beams deform as intended. The magnitude of ξ would not influence the modeling result.

Moreover, in real-world scenarios, both aforementioned buckling directions are plausible and challenging to predict due to various influencing factors such as manufacturing inaccuracies, load deviation, minor plastic deformations, and surface defect. However, only one buckling direction will be seen usually in a real-word application. Integrating these factors into mathematical models poses a significant challenge. In mechanisms design, achieving a desired deformation shape may involve inducing deformation based on designing an initially-curved small shape or applying small deviation load to the mechanisms.

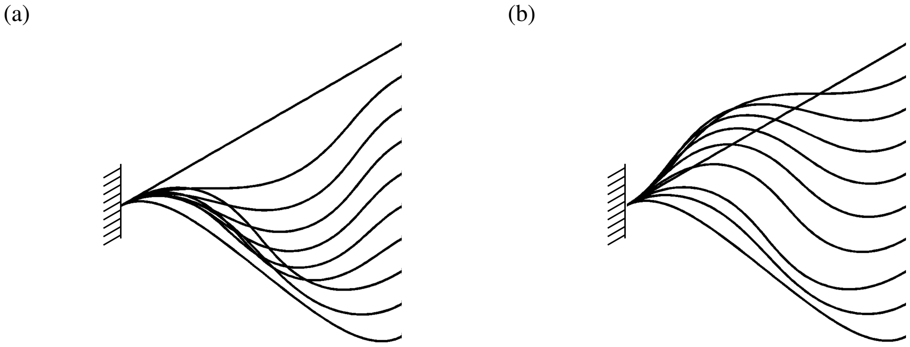

Figure 4: Two possible deformation shapes exist in modeling results. The distinct deformation shapes are induced by setting the initial guess of the root in the root-finding procedure. The sign of ξ affects the deformation shape (buckling direction). (a) Possible deformation shape A: when a positive ξ is given in initial guess $\boldsymbol{S}_0$. (b) Possible deformation shape B: when a negative ξ is given in initial guess $\boldsymbol{S}_0$.

4. FEA and experimental validation

This section focuses on validating the accuracy of the 5th-order SCME method through FEA simulations and experimental tests. The FEA simulations and experimental tests serves to further ensure the reliability of the proposed 5th-order SCME method. Details on setting up the FEA simulations and experiments are demonstrated in the following content.

4.1. FEA validation

The modeling is exemplified through the analysis of an inclined compliant beam with a length of 100 mm and an inclined angle of 20 degrees. This subsection focuses on examining the model by comparing it with FEA simulation results. The FEA simulation is conducted in Strand7 R2.4.4, a powerful commerical FEA simulation software that focuses on addressing complex issues in structural engineering and civil engineering. Its modeling and simulation capabilities enable the accurate simulation and analysis of the behavior of various structures and materials. The procedure of conducting FEA simulation is listed as:

a) Define and subdivide the compliant beam

This part involves designing the compliant beam with an initially straight shape. The beam length is set at 100 mm, and the inclined angle is designed to be 20 degrees, consistent with the modeling in the SCME method. Initially, the coordinates of the beam ends are defined as $[0, 0, 0]$ and $[100 \cos 20°, 100 \sin 20°, 0]$. The beam is then created by connecting these two nodes. When applying finite element method, the beams are normally subdivided into finite amount of beam elements (denoted as n_{FEA}). This amount (n_{FEA}) is a key factor influence the convergence and efficiency. To determine the optimal amount of beam elements, a convergence analysis is preliminary conducted as can be seen in Appendix D. Based on the convergence analysis results, the optimal number of beam elements is determined to be 200. Thus, the number of nodes in the simulation is 201. The element used for simulation in Strand7 refers to the conventional beam element with six degrees of freedom at each node: three translations and three rotations. The undeformed element is a straight line between the two nodes to which it is connected. The beam carries axial force, torque, shear forces, and bending moments in its principal planes. For modeling slender beams, the FEA simulation conducted in Strand7 is based on the planar stress assumption.

b) Define the constraint

   The constraint is the same as the constraint set in the SCME method. The beam root is fixed, restraining all degrees of freedom, while the other end is set to have movement only along the y-direction. All other degrees of freedom, including rotation along X,Y,Z axes and translational movement along X and Z axes, are fully constrained.

c) Define the mechanical properties of material

   To maintain consistency with the SCME method, Young's modulus is defined as 2800 MPa. Since we don't consider the effect caused by plate stress, we do not need to define the Poisson ratio for further calculation. The beam cross-section is set to be the same as that used in the SCME method, indicating that the width W=10mm and beam thickness T=0.6mm. All sub-beams are defined with the same material properties.

d) Conduct nonlinear static simulation

   The nonlinear static simulation only considers geometric nonlinearity while ignoring material nonlinearity. In the SCME method, 201 trajectory points are defined to obtain the applied force-displacement relationship. To maintain consistency, the nonlinear FEA is defined with 201 steps, and each step solves for the same equilibrium configuration of the compliant beam as in the SCME method. The solver for nonlinear static simulation is also based on the Newton-Raphson method. The convergence of displacement and force is set to be the same as in the SCME method, which is 10^{-14}. To avoid singularity, the function of the sub-step is applied to obtain a more accurate result when the model is hard to converge.

The procedure for conducting the simulation is outlined above, and the results obtained from the FEA simulation are compared with those from the 5th-order SCME method in Fig. 5. Noting that linear deformation compensation has been considered, based on the compensation method outlined in Appendix C.

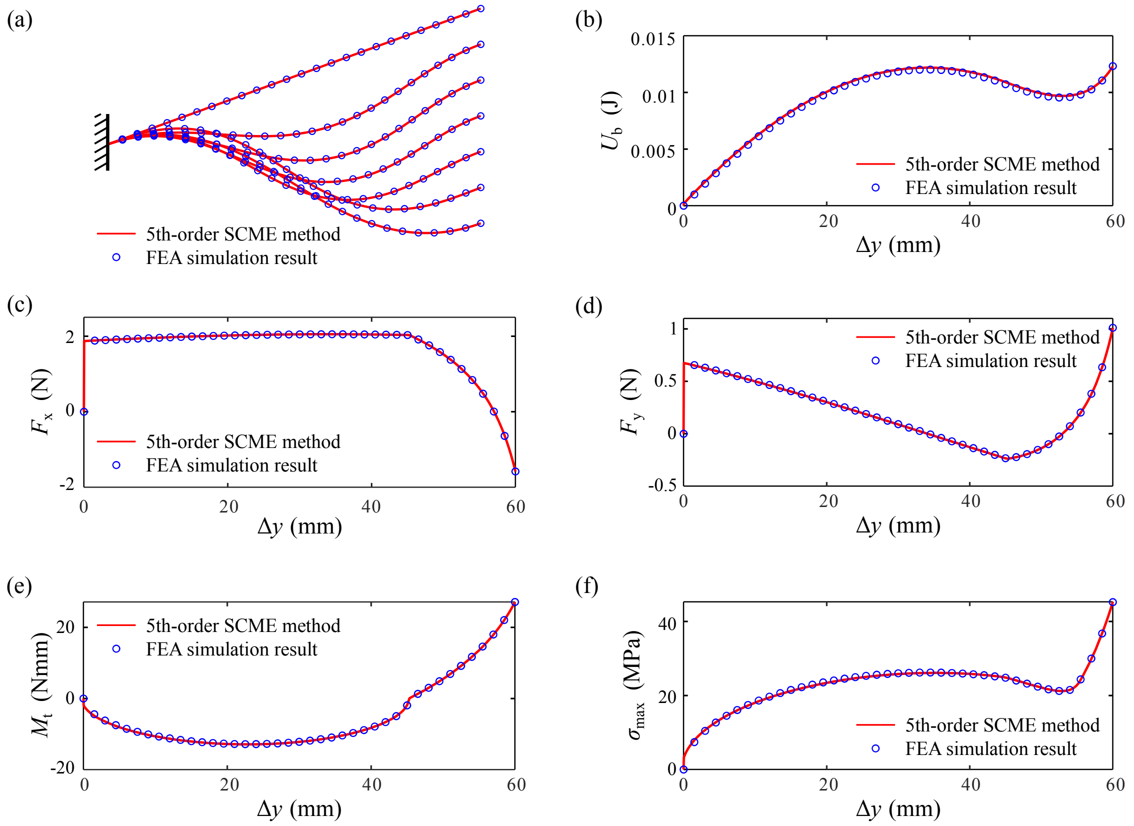

Figure 5: The modeling result comparisons between 5th-order SCME method and FEA simulation result. The parameters used in modeling and simulation are: L=100mm, θ=20°, E=2800 MPa, W=10mm, T=0.6mm. (a) Comparison of deformation shape. (b) Comparison of bending strain energy U_b. (c) Comparison of F_x (d) Comparison of F_y. (e) Comparison of M_t. (f) Comparison of maximum stress σ_{max}.

When comparing the deformation shape of the beam, as depicted in the Fig.5 , it is evident that they exhibit similar characteristics. Regarding other aspects, such as bending strain energy, applied forces, and moments, these also appear to align closely.

4.2. *Experimental validation*

In this subsection, the primary objective is to conduct an experiment test aimed at validating the accuracy of the SCME method. Through this empirical investigation, the emphasis is on providing robust confirmation of the method's accuracy in modeling the applied force and deformation shape.

4.2.1. *Model design*

The designed bistable mechanism for experimental validation is composed of four inclined compliant beams, exhibiting symmetry along the central shuttle with two beams positioned on each side. The inclusion of four beams in the design serves the purpose of mitigating the prevalent issue of rotational imbalance that often encountered in bistable mechanisms that employ only two beams. This mitigation is achieved by constraining the degrees of freedom of the mechanism, thereby ensuring its operation as a single-degree-of-freedom (DOF) mechanism. The shape and dimensions of the 3D model are illustrated in Fig. 6.

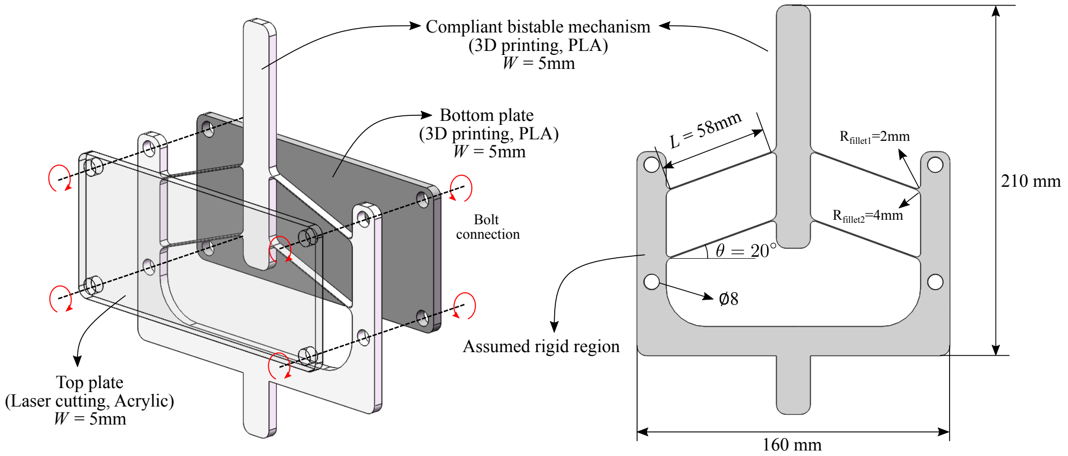

Figure 6: A prototype with three layers used for experimental validation. The bottom plate and top plate are designed to ensure sufficient stiffness of the rigid components while maintaining the entire mechanism in a relatively compact size. The middle layer is compliant bistable mechanism. Laser cutting is applied to manufacture the top plate, and transparent acrylic material is used to guarantee the visibility of deformation. The geometric parameters of the compliant bistable mechanism can be observed on the right side. Fillets are applied to the roots of beams to avoid stress concentration problems. The beam in-plane thickness T is designed to be 0.8mm.

In the SCME method, it is assumed that the root of the compliant beam is fully fixed. However, during experiments, the root is not fully constrained due to slight deformations within the assumed rigid region and further cause experimental errors. To address this, a three-layer layout is implemented to improve the stiffness of the assumed rigid region. To guarantee visibility of the deformation in the compliant bistable mechanism, the top plate is made from transparent material Acrylic, manufactured using laser cutting machine, while the bottom plate is 3D printed using black material to enhance contrast and further improve visibility. These three layers are connected via bolt connections. The center shuttle of the compliant bistable mechanism is designed to be sufficiently long to prevent interference between the mechanism and the testing machine fixture.

4.2.2. 3D printing parameters

The 3D printing process is accomplished using the UltiMaker S3 which is a fused deposition manufacturing device. This budget-friendly desktop 3D printer provides reliable performance and high-quality prints, making it ideal for prototyping. The 3D model is sliced to be further printed in UltiMaker Cura. The printing settings, including the compliant bistable mechanism and bottom plate, can be found in Tab. 2.

Table 2: Configuration for 3D printing

	Print core	Material	Infill density	Infill pattern	Temperature	Speed	Layer height	Adhesion
Compliant bistable mechanism	AA 0.25	Tough PLA	80%	Grid	210°	60mm/s	0.1mm	Skirt
Bottom plate	AA 0.4	Tough PLA	40%	Grid	210°	60mm/s	0.2mm	Skirt

Table 3: Mechanical properties of tough PLA.

	Young's modulus (MPa)	Yield stress (MPa)	Density (g/cm^3)	Hardness (Shore D)
Tough PLA	2800 (2797±151)	45.3±2	1.22	Shore D 80

Tough PLA was chosen as the preferred 3D printing material for compliant bistable mechanism due to its advantageous combination of strength, rigidity, and moderate elasticity. UltiMaker Tough PLA for S series is a technical

PLA material with a toughness similar to ABS. The mechanical properties of Tough PLA can be obtained from Table 3. It is ideal for printing functional prototypes and tooling at larger sizes, without fear of delamination or warping [79].

The top plate is chosen to be made of transparent acrylic material for visualization purposes. It is cut from an acrylic plate using a laser cutting machine (Laserscript LS1290 Pro) equipped with an 80W CO2 laser. The bed size of the laser cutting machine is 1200 x 900mm. In the cutting process, the speed is set to 5mm/s, and the laser is adjusted to 60% of its maximum power. The resulting top plate exhibits high accuracy compared to the designed model.

4.2.3. Experiment test

The experiment was conducted using the TA HD plus texture analyzer. Texture analysis involves studying how materials change mechanically, such as deforming, breaking, or undergoing other alterations when forces are applied. In this study, the texture analyzer assesses the force-displacement of a compliant bistable mechanism.

The TA HD plus can execute a single DOF movement while maintaining high accuracy in measuring force or displacement. Due to the inherent snap-through behavior in bistable mechanisms, the experiment focuses on a displacement-driven test. The prototype is positioned at the center of the texture analyzer, and displacement occurs from top to bottom. As the displacement increases, the bistable mechanism begins to deform.

The test machine records forces from sensors and to achieve a higher-resolution experimental result, a 50N load cell is chosen for the texture analyzer, with a force sensor resolution of 0.001N. The input displacement resolution is 0.001mm. To minimize dynamic effects, the movement speed is set at 0.1 mm/s. The experimental procedure is repeated five times to obtain an average value. The experimental set up can be found in Fig. 7.

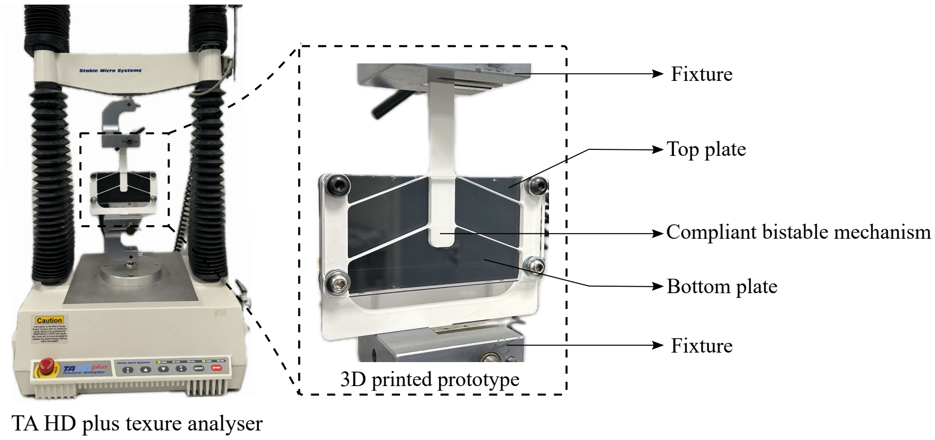

Figure 7: The experiment setup and 3D printed prototype. The experiment is conducted on the TA HD plus texture analyzer. The 3D printed prototype consists of three layers, including top and bottom plates, which are used to enhance the lateral stiffness. The middle layer is the 3D printed compliant bistable mechanism.

4.2.4. Experimental results

In the experiment, we acquired data on the force-displacement relationship and simultaneously recorded the deformation process of the compliant bistable mechanism. We compared the deformation shape at displacements of 5mm, 10mm, and 15mm, respectively. The deformation exhibited by the prototype was compared with the deformation shape predicted by the SCME method, revealing a high level of agreement. Moreover, the force-displacement data captured for the compliant bistable mechanism aligns well with both FEA simulation and SCME method predictions. These findings underscore the consistency between our experimental observations and the predicted behavior of the mechanism. The result comparison is shown in Fig. 8. The initial linear deformation is accounted for in the modeling results of the 5th-order SCME method, following the approach outlined in Appendix C.

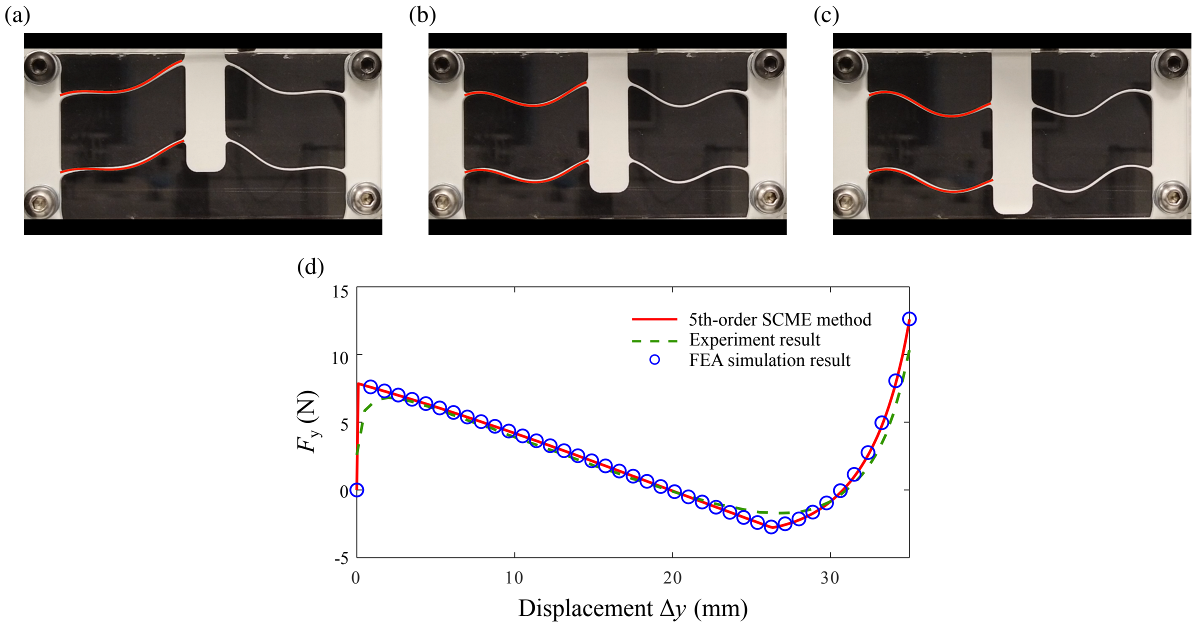

Figure 8: Experiment result comparison. The red continuous line represents the predicted deformation shape obtained from the SCME method. (a) Deformation shape comparison when Δy = 5mm. (b) Deformation shape comparison when Δy = 15mm. (c) Deformation shape comparison when Δy = 25mm. (d) Force-displacement relationship comparison among the SCME method, experiment, and FEA simulation. Note that the total force obtained through the 5th-order SCME method is four times the force calculated for a single compliant beam. This is because the designed prototype incorporates four beams.

The primary source of error stems from the insufficient rigidity of the support structure in the experiment, where deformation within the rigid region contributes to a flatter experimental force-displacement curve.

5. Discussions

A comprehensive procedure for modeling deformation shape, energy, stress, and force-displacement relationships has been established. There is a necessity to delve into the capability of the proposed high-order SCME method from the following aspects is necessary. Firstly, the order effect of the smooth curvature model is explored, as it significantly influences modeling accuracy. Secondly, the SCME method is compared with other representative modeling methods, and the results prove that the SCME method is an accurate and quick modeling method. Furthermore, the comparison also indicates that the SCME method is capable of modeling compliant beams with inclined angles varying from 0 degrees to 90 degrees. Additionally, we conduct a discussion about several limitations of the proposed SCME method, including only considering plane modeling, neglecting out-of-plane buckling, neglecting axial, shear, and twist strain energy, and assuming planar stress. The details of the discussion are available in the following content.

5.1. Effect of SCME order on modeling accuracy

Order of a smooth curvature model denotes the highest order of Legendre polynomials employed in the curvature representation process (Eq.2). A low-order model can usually advance the computational efficiency but can not meet the accuracy requirement. Generally, when dealing with intricate curvature profiles necessitating fitting, opting for a higher-order model is often the preferable choice. This preference stems from the fact that higher-order Legendre polynomials are more adaptable to closely approximate the actual curvature, particularly in cases where curvature exhibits complexity. Although the higher-order model leads to more accurate results, it would cause complex mathematical expression as well.

The compliant bistable mechanisms, with inclined angles varying from 0 to 90 degrees, are modeled using the 2th-order, 3th-order, 4th-order and 5th-order SCME methods. The modeling plotting results can be seen in Appendix

E. The modeling outcome demonstrates that when the 2nd or 3rd order is selected, the accuracy of the modeling is quite low, indicating that these two models cannot be used for modeling compliant bistable mechanisms. For the 4th-order SCME method, the overall accuracy is high and stable in the interval of angles varying from 0 to 40 degrees. However, when the beam inclined angle exceeds 40 degrees, the accuracy starts to decrease, although it can still accurately predict the force-displacement relationship in the initial region of displacements. When the order of the SCME method is increased to the 5th order, its accuracy would be much higher than the 4th-order SCME method over the full range of incined angles, and would be sufficient.

The modeling error is further assessed using normalized mean absolute error (NMAE) which is a metric used to evaluate the accuracy of models [80]. NMAE is calculated by dividing the MAE by the range of the observation values. NMAE values can range from 0 to 1, with a lower value indicating a better fit. The NMAE can be formulated using Eq. 36:

$$\mathrm{NMAE} = \frac{\frac{1}{N_i}\sum_{i=1}^{i=N_i}|F_i - \hat{F}_i|}{\max(F_i) - \min(F_i)}, \tag{36}$$

where, $\hat{F}_i$ represents the modeling results from the various modeling methods; F_i represents the observed value, which is the FEA simulation result. N_i denotes the amount of data points, corresponding to the amount of trajectory points. The NMAE has been measured for each SCME method, and the resulting data are demonstrated in Fig. 9.

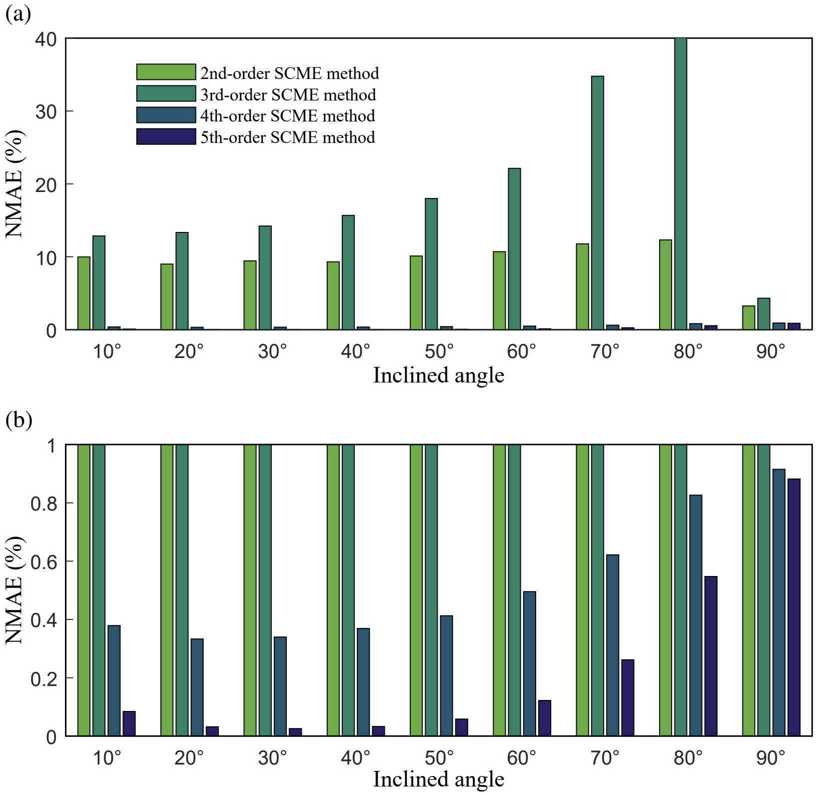

Figure 9: Modeling error comparison among 2nd-, 3rd-, 4th-, and 5th-order SCME methods. The error is measured using normalized mean absolute error. The comparison result indicates that the 5th-order SCME method is the most accurate. (a) The range of NMAE varies from 0% to 40%. (b) The range of NMAE varies from 0% to 1%.

The 5th-order SCME method has a decreasing accuracy after 40 degree but a stably high accuracy over 0 to 40 degrees. The bar chart in Fig. 9. further confirms that the 5th-order SCME method is much better than the 4th-order in terms of accuracy over the full range of angles. Overall, as the inclination angle increases, the accuracy decreases across all SCME methods accordingly, including 2nd, 3rd, 4th, and 5th order.

Table 4: Computational efficiency comparison when the trajectory has 200 sampling points ($N_i = 200$).

Inclined angle (θ)	10°	20°	30°	40°	50°	60°	70°	80°	90°	Variable Count
2th-order SCME method	0.054	0.052	0.056	0.058	0.064	0.066	0.068	0.075	0.065	6
3th-order SCME method	0.209	0.052	0.049	0.053	0.051	0.048	0.046	0.022	0.034	7
4th-order SCME method	0.115	0.021	0.018	0.022	0.024	0.022	0.023	0.022	0.018	8
5th-order SCME method	0.075	0.074	0.079	0.081	0.085	0.096	0.105	0.111	0.097	9

The computational efficiency is measured by seconds. The computation is implemented by MATLAB R2022b.

Higher-order SCME methods generally require more computation time compared to lower-order methods. Table. 4 compares the computational efficiency of SCME methods at various inclined angles, using a trajectory with 200 sampling points. Table. 4 suggests that the 5th-order SCME method can offer the best accuracy without compromising the computational efficiency too much.

5.2. *Comparative analysis of modeling methods*

Performing comparative analysis is crucial when proposing a novel method against existing modeling methods. In this subsection, we compare the SCME method with CBCM[55] and CPRBM[42], focusing mainly on modeling accuracy and computational efficiency.

In the SCME method, bending strain energy is modeled using a constructed continuous function of curvature, where the equilibrium configuration is obtained by minimizing the strain energy. The number of variables depends on the order of SCM, requiring i+3 variables for an i-th order SCM. Additionally, the SCME method provides explicit gradients, significantly speeding up the computation process.

For CBCM, the beam is divided into n elements, and BCM is applied to each element. CBCM can account for axial deformation and bending strain energy, making it better suited for modeling large deflection compliant mechanisms in which the beam undergoing axial deformation. Typically, CBCM accounts for $6n$ variables, encompassing load variables (F_x, F_y, M_t) and displacement variables (X, Y, θ). However, when applying CBCM to model compliant bistable mechanisms, the number of variables to be calculated reduces to $3n$: F_x, F_y and M_t). This is because the displacements are constrained, meaning that X, Y, θ serve as inputs to the model.

CPRBM, used for modeling large-deformation beams, treats each element as a rigid rod with a torsional spring attached to its end. The total strain energy is calculated by summing the strain energy stored in each torsional spring. CPRBM simplifies the modeling process compared to SCME and CBCM because all strain energy formulations are linear. The determination of minimum strain energy is based on an optimization strategy, with the number of variables being the deflection angle of each element. If the beam is divided into n elements, n variables need to be solved.

The compliant beams, with inclined angle ranging from 0 to 90 degrees, are modeled using the these three methods mentioned above. Then, the obtained modeling results are compared to provide a clear visualization of modeling accuracy for each method. When modeling the beams with the CBCM and CPRBM, 10 and 20 elements are employed for each model plotting to assess the computational effort and accuracy of these models. The comparison of modeling results is illustrated in Appendix F. The bar errors can be observed in Fig. 10.

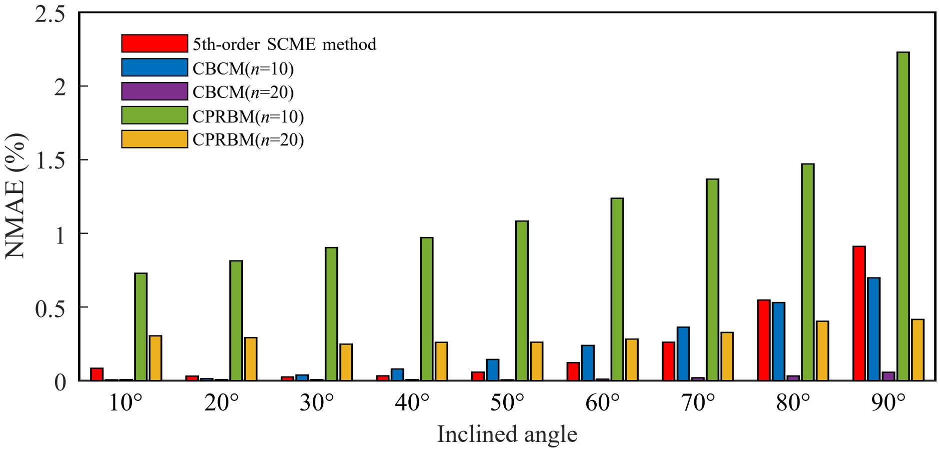

Figure 10: Modeling error comparison among the 5th-order SCME method, CBCM, and CPRBM. Ten and twenty beam elements are used in CBCM and CPRBM. The inclined angles gradually increase from 10 to 90 degrees.

The computational efficiency is measured by the computation speed of the model codes running on the same computer. The computer utilized for this research comprises a desktop equipped with an Intel Core i7-9700 3.0GHz processor, 32GB of DDR4 RAM, and an AMD Radeon RX 550 graphics card. The MATLAB version is R2022b, operating on Windows 10 enterprise edition. The computer The running time can be seen in Table. 5.

Table 5: Computational efficiency comparison when the trajectory has 200 sampling points (N_i = 200).

Inclined angle (θ)	10°	20°	30°	40°	50°	60°	70°	80°	90°	Variable Count
5th-order SCME method	0.075	0.074	0.079	0.081	0.085	0.096	0.105	0.111	0.097	9
FEA simulation	64	66	86	74	68	74	77	69	94	-
CBCM (n=10)	23.166	23.712	24.768	23.614	24.291	25.889	24.267	22.996	21.794	30
CBCM (n=20)	56.013	58.814	59.699	59.712	56.023	59.015	59.462	62.535	56.043	60
CPRBM (n=10)	11.946	11.892	11.794	11.193	11.463	11.497	11.062	10.953	10.934	10
CPRBM (n=20)	20.107	21.451	21.328	20.842	20.646	20.872	21.133	20.773	18.922	20

The computational efficiency is measured by seconds. The computation is implemented by MATLAB R2022b.

The comparison results demonstrate that the SCME method offers the advantage of the fastest modeling speed while maintaining a high level of accuracy. The SCME method stands as the second most accurate approach in the proposed list of methods. However, while the most accurate method is CBCM with 20 elements, the 5th-order SCME method exhibits a speed advantage of approximately 750 times faster than CBCM (n=20). The modeling speed of 5th-SCME method is fast due to two main reasons: Firstly, there are fewer variables to solve compared to CBCM, CPRBM, and FEA simulations. Secondly, the explicit gradient is provided when applying the Newton-Raphson method to solve for the approximate root. Thus, utilizing the SCME method can significantly reduce the time cost in the design and optimization of compliant mechanisms.

5.3. Limitations of high-order SCME method

The limitations of the proposed high-order SCME method is discussed in this subsection.

5.3.1. Plane kinetostatic modeling

For kinetostatic modeling, we have reviewed previous methods outlined in the literature, which primarily focus on plane kinetostatics for modeling mechanisms deformed in a 2D plane. Additionally, for specific applications such as MEMS, there is focus on in-plane fabrication and kinetostatics. If investigating out-of-plane deformation becomes necessary, spatial modeling technology should be considered instead of relying solely on plane modeling technology. It is essential to recognize that the current high-order SCME method lacks the capability to model spatial deformation, including spatial twist and bending, thus rendering it inadequate for spatial kinetostatic modeling.

5.3.2. Neglection of out-of-plane buckling

Out-of-plane buckling refers to the buckling behavior that occurs outside the principal deformation plane of a structure. It can result from various factors such as non-axial loads, surface defects in the beam, and material anisotropy caused by uneven material distribution. This type of buckling typically exhibits complex nonlinear characteristics, making accurate prediction challenging using mathematical methods. Many existing modeling approaches simplify analysis and design by disregarding out-of-plane buckling [42, 55, 66]. The assumption of neglecting out-of-plane buckling also applies to the SCME method.

5.3.3. Neglection of axial, shear and twist strain energy

In the process of minimizing strain energy, the optimization process is confined to bending strain energy. When modeling the post-buckling behavior of slender compliant bistable mechanisms, axial strain energy is neglected due to its small magnitude compared to bending strain energy. In the linear deformation stage, axial deformation dominates, and we compensate using Hooke's Law and the Pythagorean theorem. Shear strain energy is accounted for in modeling thick beams but ignored in slender beams. The Timoshenko-Ehrenfest beam theory, commonly used for thick beams, incorporates shear deformation and bending effects. However, in modeling compliant bistable mechanisms, the shear effect is negligible due to the use of the slender beams. Twist strain energy is not considered in modeling compliant bistable mechanisms, as all deformations are assumed to occur within a single plane, neglecting out-of-plane effects.

5.3.4. Planar stress assumption

In this work, the modeling process relies on the planar stress assumption where the Young's modulus E of the material is adopted, as reported in most papers in literature [81–83]. In the planar stress assumption, stress occurs only in the bending plane (XY-plane), and the beam's out-of-plane thickness W is qualitatively assumed to be small enough. Both the proposed high-order SCME method and FEA simulations utilize Young's modulus when modeling compliant bistable mechanisms.

When the out-of-plane thickness W is qualitatively large enough, the planar strain assumption should be considered, where the plate modulus $E' = E/(1-\nu^2)$ is adopted to [84, 85]. In the planar strain assumption, the strain perpendicular to the bending plane is negligible.

6. Conclusion

This study offers significant practical implications and contributes to the broader field of compliant mechanism design. Our proposed method, which focus on accurate planar kinetostatic modeling with wide applicability to large-deformation, straight, and curved beams, offers new opportunities for innovative designs. Additionally, the high efficiency of our model, facilitated by utilizing a low-dimensional model (without discretization) and providing explicit expressions of gradients during the root-finding algorithm, can save substantial time in optimization processes, potentially reducing costs and increasing productivity.

By extending the design space (i.e. inclined angle range in the bistable mechanism), our method inspires the creation of designs that were previously unattainable or challenging to achieve using traditional models, thus fostering innovation in mechanism design. The proposed high-order SCME method accurately delivers kinetostatic model, providing engineers with precise insights into the nonlinear behavior of compliant mechanisms, which is essential for optimizing performance and ensuring reliability in precision engineering applications. Besides, the proposed method holds promise for modeling the nonlinear energy behavior of lattices in mechanical metamaterials such as transition wave. By accurately capturing the intricate interactions within these materials, our model contributes to advancements in the development of artificial mechanical metamaterials with programmable properties and functionalities.

For future research, we have identified two key directions for advancing our work:

Firstly, we plan to enhance the accuracy and universality of the proposed SCME method. The enhancement would including exploring the potential coupling effect among various types of strain energy and try to decouple them. Through decoupling strain energy, the enhanced SCME method would be capable of modeling spatial Euler-Bernoulli beam with axial, bending, shear and twist deformation. Modeling the complex strong nonlinear spatial deformation is challenge due to increased dimensions, intricate geometry, complex loading, and higher computational complexity compared to planar modeling. Additionally, the efficiency of the SCME method could be further improved by employing advanced numerical methods such as the Newton-Raphson method with adaptive step size, which enhances the stability and convergence speed of the algorithm through dynamic adjustment of the iteration step size.

Secondly, we aim to broaden the application scenarios of the high-order SCME model which are not limited to the tip loading analysis. The proposed SCME method holds promise for modeling uniform distributed loads on cantilever beams since it is capable of considering multiple loads simultaneously. This allows us to equivalently replace the uniform distributed load by a set of closely spaced equivalent forces acting on the beam. By minimizing the strain energy under these collective load constraints, the problem of uniform distributed loads can be addressed effectively. Furthermore, the SCME method's capability to determine the deformation shape of compliant beams holds significant promise for applications in modeling contact-aided designs. This functionality would be achieved through adaptive adjustment of the constraint conditions during the deformation process.

Appendix A. Shifted Legendre polynomials

In the formulation of the SCME method, the point s is defined on the compliant beam, and thus $s/L = [0, 1]$. To simplify the formulation, we use $x = s/L$ to introduce the Legendre polynomials.

Table A.1: The shifted Legendre polynomials

N	Shifted Legendre polynomials
0	1
1	$2x - 1$
2	$6x^2 - 6x + 1$
3	$20x^3 - 30x^2 + 12x - 1$
4	$70x^4 - 140x^3 + 90x^2 - 20x + 1$
5	$252x^5 - 630x^4 + 560x^3 - 210x^2 + 30x - 1$

Table A.2: The integration of shifted Legendre polynomials

N	Integration of shifted Legendre polynomials
0	x
1	$x^2 - x$
2	$2x^3 - 3x^2 + 1$
3	$5x^4 - 10x^3 + 6x^2 - x$
4	$14x^5 - 35x^4 + 30x^3 - 10x^2 + x$
5	$42x^6 - 126x^5 + 140x^4 - 70x^3 + 15x^2 - x$

Appendix B. Gauss–Legendre quadrature

Gauss-Legendre quadrature is a numerical integration method widely employed to approximate definite integrals. It relies on the principle of estimating the integral through a weighted sum of function values at specific points within the integration interval. Renowned for its accuracy and efficiency in numerical integration, Gauss-Legendre quadrature finds particular utility in integrating smooth functions over finite intervals. Its applications span diverse disciplines, encompassing physics, engineering, and numerical analysis, where precise numerical integration holds paramount importance. The expression for Gauss-Legendre quadrature is as follows:

$$\int_{-1}^{1} f(x)dx \approx \sum_{i=1}^{i=n} W_i f(x_i), \tag{B.1}$$

where, $f(x)$ is the function being integrated. dx denotes the differential element. $\sum_{i=1}^{i=n}$ represents the sum over the quadrature points. x_i represents the quadrature points within the interval [-1, 1]. To avoid confusion, the quadrature point in this paper is represented by s_k. W_i represents the corresponding weights assigned to each quadrature point. To avoid confusion, the weight in this paper is represented by Δk.

The Legendre polynomials, originally defined on the interval [-1, 1], serve as the foundation for Gauss-Legendre quadrature. However, to apply this quadrature method to a general interval [a, b], a transformation process is required. This transformation involves mapping the original interval [-1, 1] to the desired interval [a, b]. The expression for Gauss-Legendre quadrature on the interval [a, b] can be formulated as:

$$\int_{a}^{b} f(x)dx \approx \frac{b-a}{2} \sum_{i=1}^{i=n} W_i f\left(\frac{b-a}{2}x_i + \frac{a+b}{2}\right). \tag{B.2}$$

In the context of the smooth curvature model, the variable is denoted as s/L, where s represents the distance along the curve and L is a length of compliant beam. In this model, s/L is constrained within the interval [0, 1]. Therefore, for the specific case of integrating over the interval [0, 1], the Gauss-Legendre quadrature can be expressed as follows, where $a = 0$ and $b = L$:

$$\int_{0}^{L} f(x)dx \approx \frac{L}{2} \sum_{i=1}^{i=n} W_i f\left(\frac{L}{2}x_i + \frac{L}{2}\right). \tag{B.3}$$

In the smooth curvature model, when using the Gauss-Legendre quadrature with 5 points to calculate integration over the interval [0, 1], the corresponding weights and quadrature points are listed as follows:

Table B.1: The weights and quadrature points

n	quadrature point (x_i)	weight (W_i)
1	-0.9739065285171717	0.0666713443086881
2	-0.8650633666889845	0.1494513491505806
3	-0.6794095682990244	0.2190863625159820
4	-0.4333953941292472	0.2692667193099963
5	-0.1488743389816312	0.2955242247147529
6	0.1488743389816312	0.2955242247147529
7	0.4333953941292472	0.2692667193099963
8	0.6794095682990244	0.2190863625159820
9	0.8650633666889845	0.1494513491505806
10	0.9739065285171717	0.0666713443086881

Hence, when we aim to integrate the equation and subsequently obtain the tip position and orientation, we can employ the Gauss-Legendre quadrature method by substituting the function $f(x)$ with the target function. By utilizing the appropriate weights and quadrature points, we can approximate the integral and derive the desired tip position and orientation which is formulated in Eq. (B.4) (B.5) and (B.6):

$$\phi_{\text{tip}}(\boldsymbol{\alpha}) = \phi(\boldsymbol{\alpha}, L) = \phi_0 + \alpha_0, \tag{B.4}$$

$$\begin{aligned}
x_{\text{tip}}(\boldsymbol{\alpha}) \approx L \sum_{i=1}^{5} W_i \cos\Bigg[& \alpha_0 \left(\frac{1}{2}(x_i+1)\right) + \alpha_1 \left(\frac{1}{4}(x_i+1)^2 - \frac{1}{2}(x_i+1)\right) \\
& + \alpha_2 \left(\frac{1}{4}(x_i+1)^3 - \frac{3}{4}(x_i+1)^2 + \frac{1}{2}(x_i+1)\right) \\
& + \alpha_3 \left(\frac{5}{16}(x_i+1)^4 - \frac{5}{4}(x_i+1)^3 + \frac{3}{2}(x_i+1)^2 - \frac{1}{2}(x_i+1)\right) \\
& + \alpha_4 \left(\frac{14}{32}(x_i+1)^5 - \frac{35}{16}(x_i+1)^4 + \frac{15}{4}(x_i+1)^3 - \frac{5}{2}(x_i+1)^2 + \frac{1}{2}(x_i+1)\right) \\
& \alpha_5 \left(\frac{21}{32}(x_i+1)^5 - \frac{63}{16}(x_i+1)^5 + \frac{35}{4}(x_i+1)^4 - \frac{35}{4}(x_i+1)^3 + \frac{15}{4}(x_i+1)^2 - \frac{1}{2}(x_i+1)\right)\Bigg],
\end{aligned} \tag{B.5}$$

$$\begin{aligned}
y_{\text{tip}}(\boldsymbol{\alpha}) \approx L \sum_{i=1}^{5} W_i \sin\Bigg[& \alpha_0 \left(\frac{1}{2}(x_i+1)\right) + \alpha_1 \left(\frac{1}{4}(x_i+1)^2 - \frac{1}{2}(x_i+1)\right) \\
& + \alpha_2 \left(\frac{1}{4}(x_i+1)^3 - \frac{3}{4}(x_i+1)^2 + \frac{1}{2}(x_i+1)\right) \\
& + \alpha_3 \left(\frac{5}{16}(x_i+1)^4 - \frac{5}{4}(x_i+1)^3 + \frac{3}{2}(x_i+1)^2 - \frac{1}{2}(x_i+1)\right) \\
& + \alpha_4 \left(\frac{14}{32}(x_i+1)^5 - \frac{35}{16}(x_i+1)^4 + \frac{15}{4}(x_i+1)^3 - \frac{5}{2}(x_i+1)^2 + \frac{1}{2}(x_i+1)\right) \\
& \alpha_5 \left(\frac{21}{32}(x_i+1)^5 - \frac{63}{16}(x_i+1)^5 + \frac{35}{4}(x_i+1)^4 - \frac{35}{4}(x_i+1)^3 + \frac{15}{4}(x_i+1)^2 - \frac{1}{2}(x_i+1)\right)\Bigg].
\end{aligned} \tag{B.6}$$

Appendix C. Initial linear deformation compensation

Prior to buckling, the beam experiences linear axial deformation while maintaining its equilibrium configuration. However, once the critical buckling load is reached, the structure loses its stability and the internal stresses are no longer sufficient to balance the applied load. As a result, the structure begins to buckle laterally and its axial stiffness decreases, causing the load to be redistributed throughout the structure. To compensate the initial linear deformation occurs before the buckling happened, we have set up a nonlinear equation system to solve for the initial buckling position Δy_b. The geometric relationship can be seen from the Fig.C.1.

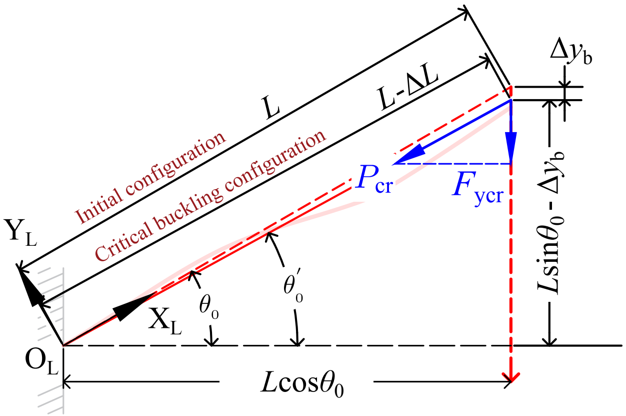

Figure C.1: The variables and geometrical parameters defined to derive the critical buckling position and force. The initial configuration of the beam is represented using the red dashed line. The critical buckling configuration is represented using the red continuous line. The buckled configuration of the beam line is represented using a half-transparent red continuous line.

The critical axial buckling force P_cr is dependent on the geometrical shape, material properties, and boundary conditions applied to the compliant beam. When modeling the compliant bistable mechanism, the critical axial buckling force P_cr has a component force F_ycr along the moving direction. The component force F_ycr can be determined through the first point on the force-displacement relationship obtained from the SCME method. By applying the Pythagorean theorem and Hooke's law, a system of two nonlinear equations can be established to solve for the critical buckling position Δy_b and the axial deformation ΔL. The axial deformation ΔL can be calculated by dividing the critical buckling force F_ycr by the axial stiffness k, which can be formulated as EA/L; where E represents the Young modulus and A denotes the cross-sectional area of the beam:

$$\begin{cases} \Delta L = \dfrac{P_\text{cr}}{k} = \dfrac{PL}{EA\sin\theta_0'} = \dfrac{PL\,(L-\Delta L)}{EA\,(L\sin\theta_0 - \Delta y_\text{b})}, \\ (L-\Delta L)^2 = (L\cos\theta_0)^2 + (L\sin\theta_0 - \Delta y_\text{b})^2 \,. \end{cases} \tag{C.1}$$

To verify the accuracy of this model under small deformation conditions, we conducted a case study involving a beam with a length of 100 mm and a thickness of 2 mm. The inclined angle is $\theta_0 = 20°$. The Young's modulus used in this case study is 2800 MPa. The response of the compliant beam is modeled within the range of $\Delta y = [0, 1]$. The comparison between linear deformation compensation and FEA simulation results can be seen from Fig. C.2. The comparison indicates agreement between the FEA simulation result and linear compensation, demonstrating the feasibility of the approach for determining the critical buckling position and force.

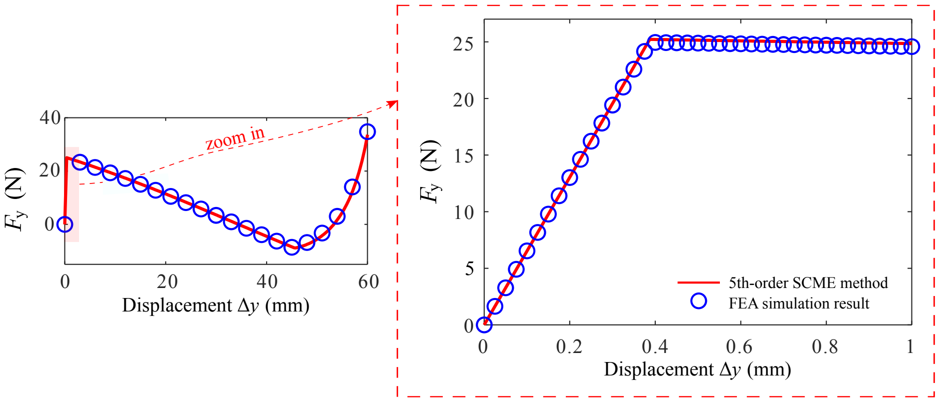

Figure C.2: Comparison between the modeling result considering linear compensation and FEA simulation. The overall force-displacement curve is displayed on the left, while the displacement range [0,1] is zoomed in to provide a clearer visualization of the linear deformation compensation result, as demonstrated on the right.

Appendix D. Convergence Analysis of FEA simulation

As a benchmark for comparison, the accuracy of FEA simulation plays a vital role since it directly affects the evaluation of other methods. This appendix introduces the procedure for determining the optimal number of beam elements when conducting FEA simulation. This is because the number of beam elements is a key factor impacting the accuracy of FEA simulation.

The details of the setup in FEA simulation can be found in Section 4.1. To investigate the effects caused by using various numbers of beam elements, several FEA simulations are conducted and their results are compared. Convergence is measured by observing the variation of the local minimum value in F_y since it is the critical point with the highest modeling challenge for the accuracy. When the force stabilizes to a certain specified value, the simulation is considered to have efficiently converged. Then, the optimal amount of beam elements can be determined by consulting with computational efficiency. The comparison results can be seen in Fig. D.1.

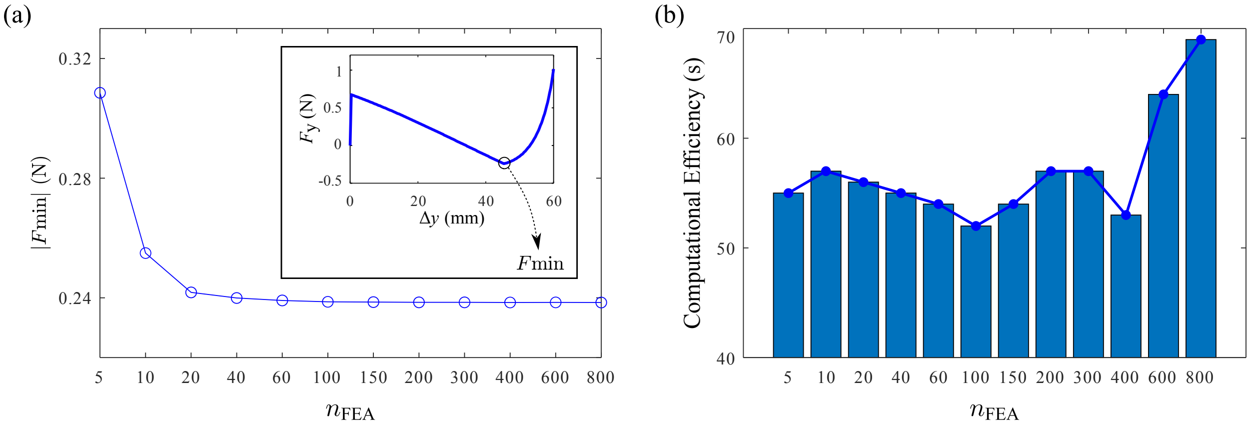

Figure D.1: Convergence analysis of FEA simulation via modeling compliant beams with varying numbers of beam elements. The amount of beam elements varies from 5 to 800. (a) The local minima of the force-displacement curve (F_{min}) obtained from FEA simulations against distinct beam elements. The convergence of the simulation is evaluated by examining whether the magnitude of F_{min} converges. (b) Computational efficiency comparison, which is measured in seconds.

Table D.1: The values of F_{min} obtained from FEA simulations when the beam are subdivided into distinct amounts of beam elements.

n_{FEA}	5	10	20	40	60	100	150	200	300	400	600	800
$\lvert F_{\text{min}} \rvert$ (N)	0.308527	0.254951	0.241803	0.239930	0.239110	0.238652	0.238559	0.238478	0.238479	0.238433	0.238456	0.238423

In table D.1, we can observe that as the number of beam elements exceeds two hundred, the force begins to converge to the fourth decimal place (converging to 0.0001N). This level of precision is sufficient for finite element simulation and can be trusted as a baseline. It is also noted from Fig. D.1 (b) that, the computational efficiency at n=200 is relatively high, however, when $n = 600$ or $n = 800$, the computational efficiency decreases significantly.

Appendix E. Force-displacement relationship comparison between distinct order SCME methods

The force-displacement relationship comparison results are presented in Fig. E.1. These results are obtained separately using the 2nd-order, 3rd-order, 4th-order and 5th-order SCME methods.

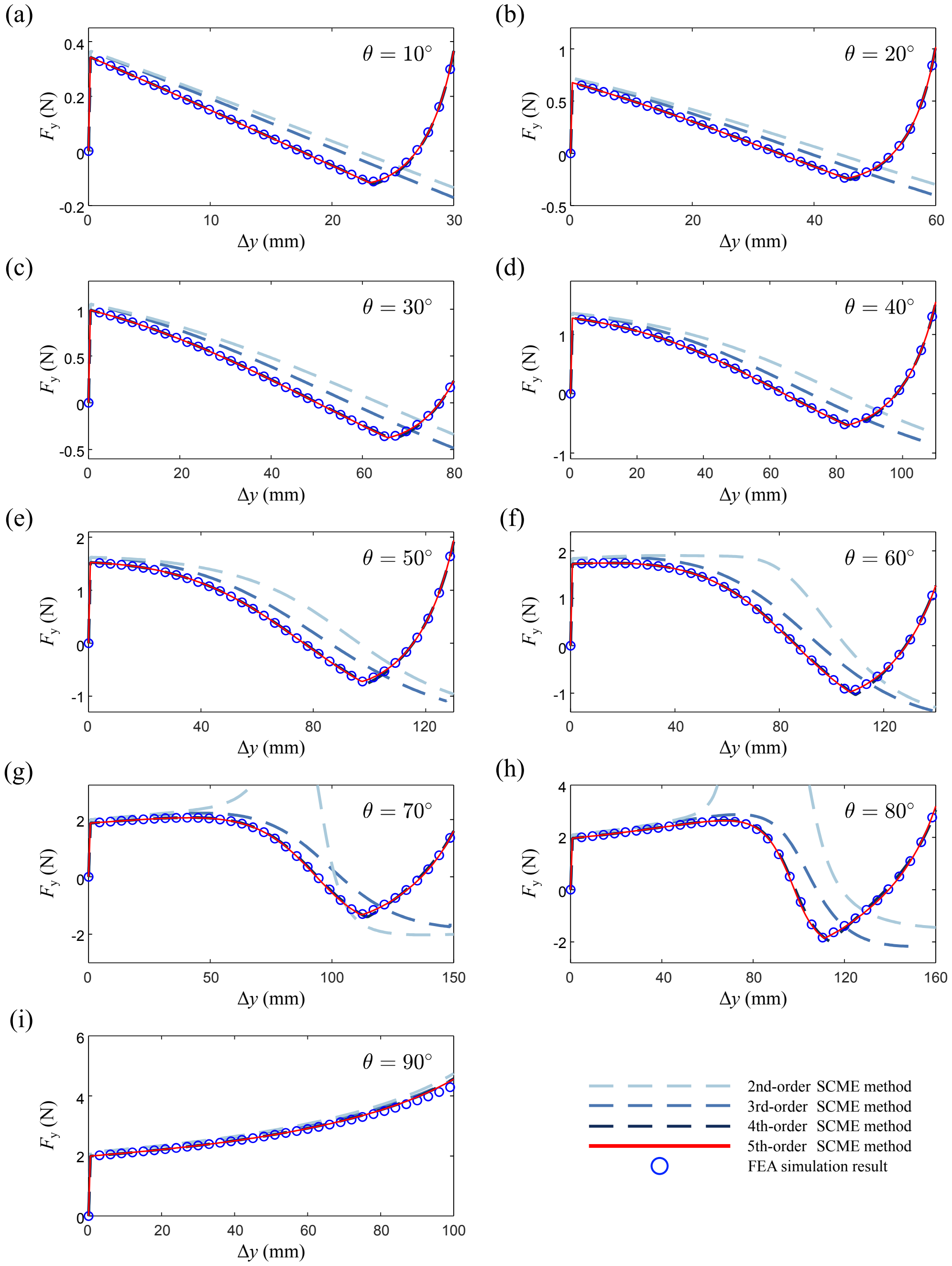

Figure E.1: Force-displacement relationship comparison between 2nd-order, 3rd-order, 4th-order and 5th-order SCME method. The parameters used in modeling and simulation are: L=100mm, E=2800 MPa, W=10mm, T=0.6mm. (a) $\theta = 10°$. (b) $\theta = 20°$.(c) $\theta = 30°$. (d) $\theta = 40°$. (e) $\theta = 50°$. (f) $\theta = 60°$. (g) $\theta = 70°$. (h) $\theta = 80°$. (i) $\theta = 90°$.

Appendix F. Force-displacement relationship comparison between distinct modeling methods

The force-displacement relationship comparison results are presented in Fig. F.1. These results are obtained separately using the 5th-order SCME method, CBCM, and CPRBM.

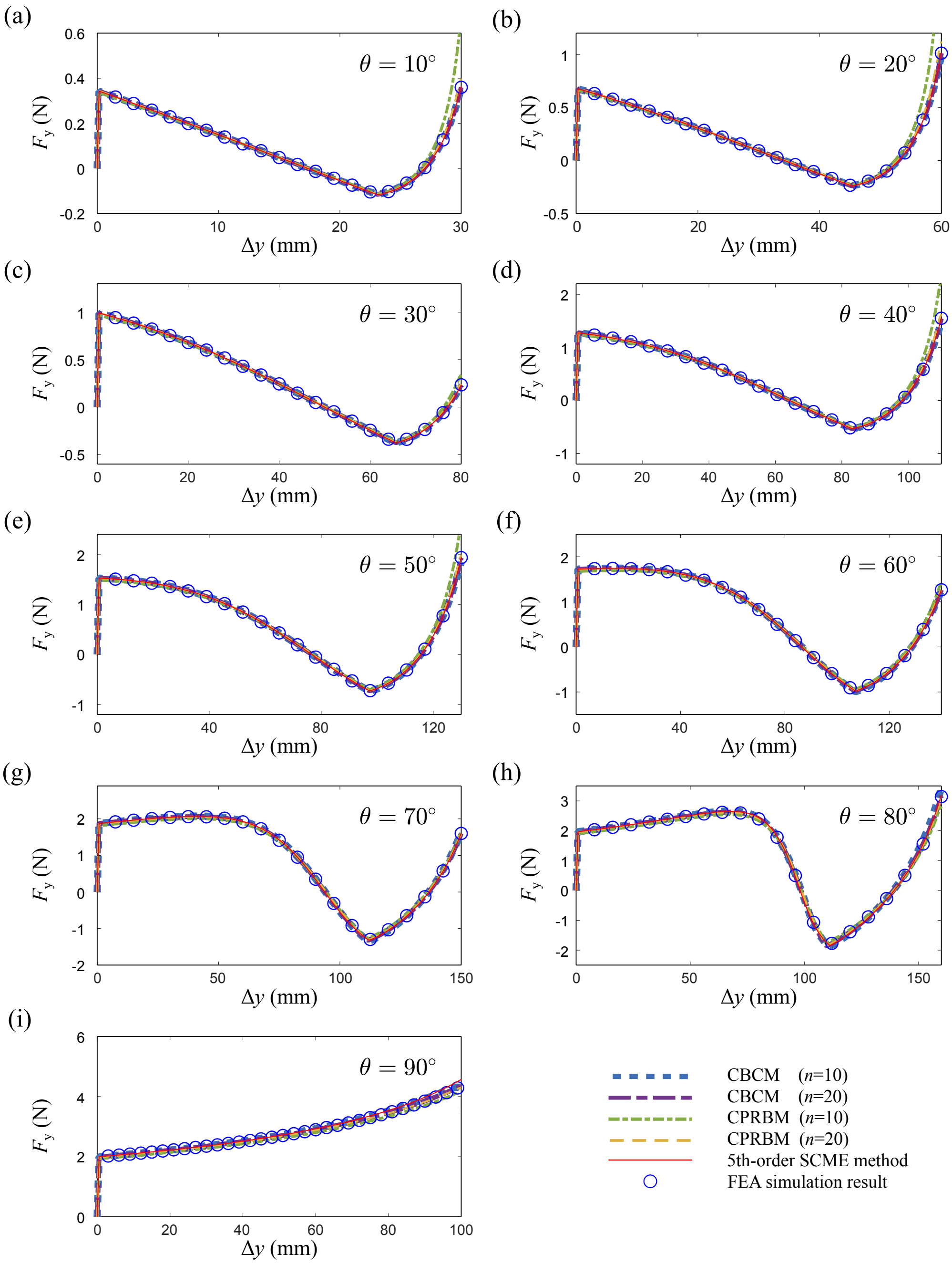

Figure F.1: Force-displacement relationship comparison between 5th-order SCME method, CBCM, CPRBM, and FEA simulation. Ten and twenty beam elements are used in CBCM and CPRBM. The parameters used in modeling and simulation are: L=100mm, E=2800 MPa, W=10mm, T=0.6mm. (a) $\theta = 10°$. (b) $\theta = 20°$.(c) $\theta = 30°$. (d) $\theta = 40°$. (e) $\theta = 50°$. (f) $\theta = 60°$. (g) $\theta = 70°$. (h) $\theta = 80°$. (i) $\theta = 90°$.

Appendix G. Solving for displacements under given loads using 5th-order SCM

This appendix outlines the procedure of solving for beam displacements under given loads using a 5th-smooth curvature model. Unlike displacement-driven modeling in section 3, which often presents multiple solutions, force-driven modeling typically results in a single solution. To illustrate, we consider the case of applying a tip constraint and that of applying to tip load. When aligning the beam tip with a specified position, there may exist multiple solutions to achieve this alignment. Each solution corresponds to a distinct magnitude of strain energy stored within the deformed beam. The configuration with minimum strain energy can lead to the solution to the displacement-driven problem. Conversely, in force-driven modeling, adhering to the principles of Euler-Bernoulli beam theory, once the load is determined, the distribution of moments along the beam can be established. With the moment distribution known, the beam's deformation can be subsequently determined. This explains why force-driven modeling typically yields a single solution.

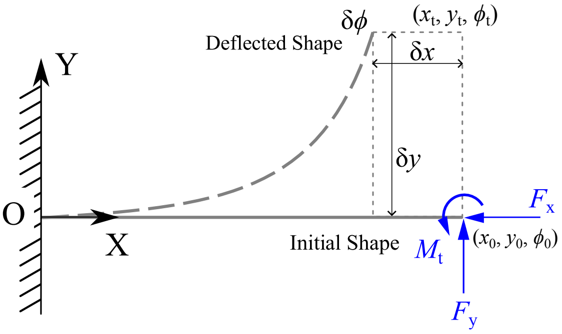

Figure G.1: Definition of parameters employed in the force-driven modeling. The initial undeflected beam is represented by a gray continuous line, while the deflected beam is represented by a gray dashed line. The beam root is fixed to the ground, loads (F_x, F_y, M_t) are applied at the beam tip, resulting in beam deflection. The beam's tip displacement is represented by δx and δy, while the deflection angle is $\delta\phi$. Initial coordinates of the beam tip are denoted as (x_0, y_0, ϕ_0), and deflected tip coordinates are denoted as (x_t, y_t, ϕ_t).

As can be seen in Fig. G.1, the coordinate of beam tip before deformation can be formulated in Eq. (G.1), Eq. (G.2) and Eq. (G.3):

$$x_0 = L, \tag{G.1}$$
$$y_0 = 0, \tag{G.2}$$
$$\phi_0 = 0. \tag{G.3}$$

The tip coordinates of deflected beam can be calculated by using Eq. (G.4), Eq. (G.5) and Eq. (G.6):

$$x_t \approx \frac{L}{2}\sum_{i=1}^{i=10} W_i \cos\left[\phi\left(\alpha, \left(\frac{L}{2}x_i + \frac{L}{2}\right)\right)\right], \tag{G.4}$$
$$y_t \approx \frac{L}{2}\sum_{i=1}^{i=10} W_i \sin\left[\phi\left(\alpha, \left(\frac{L}{2}x_i + \frac{L}{2}\right)\right)\right], \tag{G.5}$$
$$\phi_t = \alpha_0. \tag{G.6}$$

The beam deflects under a given load (F_x, F_y, M_t). The work done by external force is converted to bending strain energy (neglected other type of strain energy) stored in the deflected beam, based on the principle of energy conservation. The formulation can be obtained in Eq. (G.7):

$$
\begin{aligned}
U_{\mathrm{b}}(\boldsymbol{\alpha}) &= F_{\mathrm{x}}\delta x + F_{\mathrm{y}}\delta y + M_{\mathrm{t}}\delta\phi \\
&= F_{\mathrm{x}}\left(x_{\mathrm{t}} - x_0\right) + F_{\mathrm{y}}\left(y_{\mathrm{t}} - y_0\right) + M_{\mathrm{t}}\left(\phi_{\mathrm{t}} - \phi_0\right) \\
&\approx F_{\mathrm{x}}\left(\frac{L}{2}\sum_{i=1}^{i=10} W_i \cos\left[\phi\left(\boldsymbol{\alpha}, \left(\frac{L}{2}x_i + \frac{L}{2}\right)\right)\right] - L\right) + F_{\mathrm{y}}\left(\frac{L}{2}\sum_{i=1}^{i=10} W_i \sin\left[\phi\left(\boldsymbol{\alpha}, \left(\frac{L}{2}x_i + \frac{L}{2}\right)\right)\right]\right) + M_{\mathrm{t}}\alpha_0.
\end{aligned}
\tag{G.7}
$$

When project the energy to generalized coordinates, we can obtain the following nonlinear equation system in Eq.(G.8):

$$
\begin{cases}
\dfrac{\partial U_{\mathrm{b}}(\boldsymbol{\alpha})}{\partial \alpha_0} \approx \dfrac{\partial\left[F_{\mathrm{x}}\left(\frac{L}{2}\sum_{i=1}^{i=10} W_i \cos\left[\phi\left(\boldsymbol{\alpha}, \left(\frac{L}{2}x_i + \frac{L}{2}\right)\right)\right] - L\right) + F_{\mathrm{y}}\left(\frac{L}{2}\sum_{i=1}^{i=10} W_i \sin\left[\phi\left(\boldsymbol{\alpha}, \left(\frac{L}{2}x_i + \frac{L}{2}\right)\right)\right]\right) + M_{\mathrm{t}}\alpha_0\right]}{\partial \alpha_0}, \\
\dfrac{\partial U_{\mathrm{b}}(\boldsymbol{\alpha})}{\partial \alpha_1} \approx \dfrac{\partial\left[F_{\mathrm{x}}\left(\frac{L}{2}\sum_{i=1}^{i=10} W_i \cos\left[\phi\left(\boldsymbol{\alpha}, \left(\frac{L}{2}x_i + \frac{L}{2}\right)\right)\right] - L\right) + F_{\mathrm{y}}\left(\frac{L}{2}\sum_{i=1}^{i=10} W_i \sin\left[\phi\left(\boldsymbol{\alpha}, \left(\frac{L}{2}x_i + \frac{L}{2}\right)\right)\right]\right) + M_{\mathrm{t}}\alpha_0\right]}{\partial \alpha_1}, \\
\dfrac{\partial U_{\mathrm{b}}(\boldsymbol{\alpha})}{\partial \alpha_2} \approx \dfrac{\partial\left[F_{\mathrm{x}}\left(\frac{L}{2}\sum_{i=1}^{i=10} W_i \cos\left[\phi\left(\boldsymbol{\alpha}, \left(\frac{L}{2}x_i + \frac{L}{2}\right)\right)\right] - L\right) + F_{\mathrm{y}}\left(\frac{L}{2}\sum_{i=1}^{i=10} W_i \sin\left[\phi\left(\boldsymbol{\alpha}, \left(\frac{L}{2}x_i + \frac{L}{2}\right)\right)\right]\right) + M_{\mathrm{t}}\alpha_0\right]}{\partial \alpha_2}, \\
\dfrac{\partial U_{\mathrm{b}}(\boldsymbol{\alpha})}{\partial \alpha_3} \approx \dfrac{\partial\left[F_{\mathrm{x}}\left(\frac{L}{2}\sum_{i=1}^{i=10} W_i \cos\left[\phi\left(\boldsymbol{\alpha}, \left(\frac{L}{2}x_i + \frac{L}{2}\right)\right)\right] - L\right) + F_{\mathrm{y}}\left(\frac{L}{2}\sum_{i=1}^{i=10} W_i \sin\left[\phi\left(\boldsymbol{\alpha}, \left(\frac{L}{2}x_i + \frac{L}{2}\right)\right)\right]\right) + M_{\mathrm{t}}\alpha_0\right]}{\partial \alpha_3}, \\
\dfrac{\partial U_{\mathrm{b}}(\boldsymbol{\alpha})}{\partial \alpha_4} \approx \dfrac{\partial\left[F_{\mathrm{x}}\left(\frac{L}{2}\sum_{i=1}^{i=10} W_i \cos\left[\phi\left(\boldsymbol{\alpha}, \left(\frac{L}{2}x_i + \frac{L}{2}\right)\right)\right] - L\right) + F_{\mathrm{y}}\left(\frac{L}{2}\sum_{i=1}^{i=10} W_i \sin\left[\phi\left(\boldsymbol{\alpha}, \left(\frac{L}{2}x_i + \frac{L}{2}\right)\right)\right]\right) + M_{\mathrm{t}}\alpha_0\right]}{\partial \alpha_4}, \\
\dfrac{\partial U_{\mathrm{b}}(\boldsymbol{\alpha})}{\partial \alpha_5} \approx \dfrac{\partial\left[F_{\mathrm{x}}\left(\frac{L}{2}\sum_{i=1}^{i=10} W_i \cos\left[\phi\left(\boldsymbol{\alpha}, \left(\frac{L}{2}x_i + \frac{L}{2}\right)\right)\right] - L\right) + F_{\mathrm{y}}\left(\frac{L}{2}\sum_{i=1}^{i=10} W_i \sin\left[\phi\left(\boldsymbol{\alpha}, \left(\frac{L}{2}x_i + \frac{L}{2}\right)\right)\right]\right) + M_{\mathrm{t}}\alpha_0\right]}{\partial \alpha_5},
\end{cases}
\tag{G.8}
$$

where,

$$
U_{\mathrm{b}}(\boldsymbol{\alpha}) = \frac{EI}{2L}\left(\alpha_0^2 + \frac{\alpha_1^2}{3} + \frac{\alpha_2^2}{5} + \frac{\alpha_3^2}{7} + \frac{\alpha_4^2}{9} + \frac{\alpha_5^2}{11}\right).
\tag{G.9}
$$

By solving the nonlinear equation system in Eq. (G.8), the value of each $\boldsymbol{\alpha}$ is obtained, which is used to derive further characteristics such as the beam tip position and deformation shape. To validate this method, a case study is conducted. A straight beam is subjected to a load of $F_{\mathrm{y}} = 15$ N at the beam tip, to trigger a geometrically nonlinear deformation , while the magnitudes of F_{x} and M_{t} are both zero. The beam has a length of 100 mm, a thickness T of 0.6 mm, and a width W of 10 mm. After obtaining the results from the aforementioned modeling process, a FEA simulation is performed to verify the results. The comparison between the obtained results can be seen in Fig. G.2.

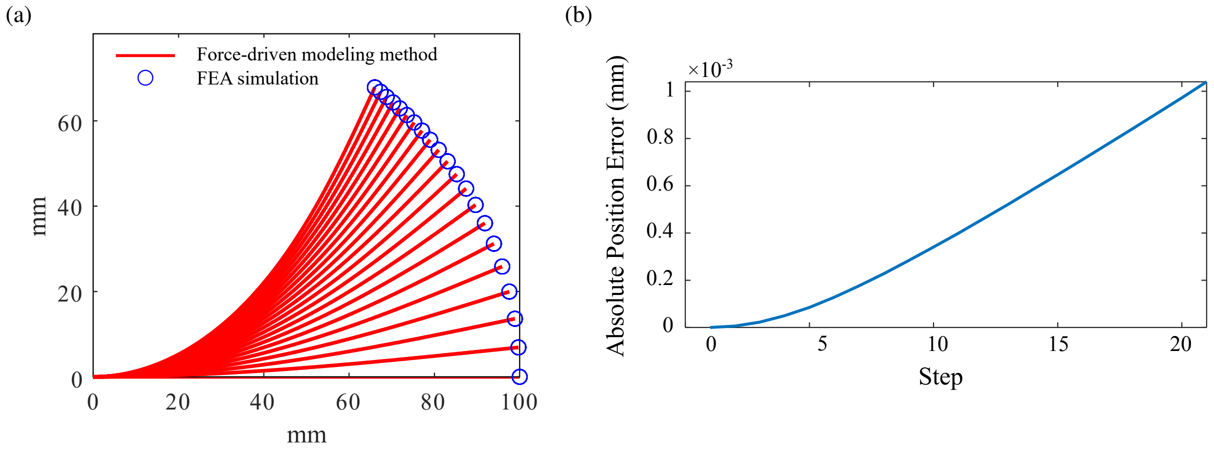

Figure G.2: Force-driven modeling result compared with FEA simulation. (a) The deformation shape comparison, with focus on the beam tip position. (b) The error between the modeling result and FEA simulation result. The error is measured using absolute positional error, which is measured by calculating the distance between the tip points obtained from modeling and FEA simulation. Step indicates the deformation process.

The comparison shown in Fig. G.2 proves that the proposed force-driven modeling method is valid for solving for displacements under given loads using the 5th-order smooth curvature model.

Declaration of competing interest

The authors declare that they have no known competing financial interests or personal relationships that could have appeared to influence the work reported in this paper.

Data availability

Data will be made available on request.

Acknowledgement

Tinghao Liu is grateful for the financial support from the China Scholarship Council (CSC Student ID: 202208300023). The authors wish to express their sincere gratitude to Mr. Timothy Power, UCC's Chief Technician, for his extraordinary and indispensable contributions to the prototyping process. The authors extend their thanks to Mr. Paul Conway for his valuable contribution to the experimental test.

References

[1] L. L. Howell, Compliant mechanisms, in: 21st Century Kinematics, Springer, 2013, pp. 189–216. `doi:10.1007/978-1-4471-4510-3_7`.
[2] P. McGowan, G. Hao, Design of a Morphing Compliant Mechanism With Separate Gripping and Retraction Modes Using a Single Actuation, Journal of Mechanisms and Robotics 15 (1) (2022) 015002. `doi:10.1115/1.4054551`.
[3] G. Hao, H. Li, A. Nayak, S. Caro, Design of a Compliant Gripper With Multimode Jaws, Journal of Mechanisms and Robotics 10 (3) (2018) 031005. `doi:10.1115/1.4039498`.
[4] M. Ling, L. Yuan, Z. Luo, T. Huang, X. Zhang, Enhancing Dynamic Bandwidth of Amplified Piezoelectric Actuators by a Hybrid Lever and Bridge-Type Compliant Mechanism, Actuators 11 (5) (2022). `doi:10.3390/act11050134`.
[5] S. Li, G. Hao, Current trends and prospects in compliant continuum robots: A survey, Actuators 10 (7) (2021). `doi:10.3390/act10070145`.
[6] S. Li, G. Hao, Y. Chen, J. Zhu, G. Berselli, Nonlinear Analysis of a Class of Inversion-Based Compliant Cross-Spring Pivots, Journal of Mechanisms and Robotics 14 (3) (2021) 031007. `doi:10.1115/1.4052514`.
[7] S. Ye, P. Zhao, S. Li, F. Kavousi, G. Hao, Modelling of a tubular kirigami (RC-kiri) with outside lamina emergent torsional joints, in: New Advances in Mechanisms, Transmissions and Applications, Springer, 2023, pp. 264–276. `doi:10.1007/978-3-031-29815-8_26`.

- [8] F. Sturm, E. Wehrle, M. Hornung, Simplified modeling of topology-optimized compliant mechanism for multi-fidelity integration in morphing wings, in: AIAA AVIATION 2023 Forum, 2023. `doi:10.2514/6.2023-4022`.
- [9] J. Achleitner, K. Rohde-Brandenburger, P. R. von Bieberstein, F. Sturm, M. Hornung, Aerodynamic design of a morphing wing sailplane, in: AIAA Aviation 2019 Forum, 2019. `doi:10.2514/6.2019-2816`.
- [10] P. Zhao, J. Liu, C. Wu, Y. Li, K. Chen, Novel surface design of deployable reflector antenna based on polar scissor structures, Chinese Journal of Mechanical Engineering 33 (68) (2020). `doi:10.1186/s10033-020-00488-6`.
- [11] P. Zhao, J. Liu, C. Wu, S. Ye, Q. Yang, G. Hao, Deployment analysis of membranes with creases using a nonlinear torsion spring model, International Journal of Mechanical Sciences 255 (2023) 108444. `doi:10.1016/j.ijmecsci.2023.108444`.
- [12] Z. Wu, Q. Xu, Design of a structure-based bistable piezoelectric energy harvester for scavenging vibration energy in gravity direction, Mechanical Systems and Signal Processing 162 (2022) 108043. `doi:10.1016/j.ymssp.2021.108043`.
- [13] H. Liang, G. Hao, O. Z. Olszewski, V. Pakrashi, Ultra-low wide bandwidth vibrational energy harvesting using a statically balanced compliant mechanism, International Journal of Mechanical Sciences 219 (2022) 107130. `doi:10.1016/j.ijmecsci.2022.107130`.
- [14] F. Qian, M. R. Hajj, L. Zuo, Bio-inspired bi-stable piezoelectric harvester for broadband vibration energy harvesting, Energy Conversion and Management 222 (2020) 113174. `doi:https://doi.org/10.1016/j.enconman.2020.113174`.
- [15] H.-W. Huang, Y.-J. Yang, A MEMS Bistable Device With Push-On–Push-Off Capability, Journal of Microelectromechanical Systems 22 (1) (2013) 7–9. `doi:10.1109/JMEMS.2012.2228165`.
- [16] H. Steiner, W. Hortschitz, M. Stifter, F. Keplinger, Thermal actuated passive bistable MEMS switch, in: 2014 Microelectronic Systems Symposium (MESS), 2014, pp. 1–5. `doi:10.1109/MESS.2014.7010249`.
- [17] N. D. Masters, L. L. Howell, A Three Degree-of-Freedom Model for Self-Retracting Fully Compliant Bistable Micromechanisms , Journal of Mechanical Design 127 (4) (2005) 739–744. `doi:10.1115/1.1828463`.
- [18] Y. Zhao, G. Hao, L. Chai, Y. Tian, F. Xi, A compliant-mechanism-based lockable prismatic joint for high-load morphing structures, Mechanism and Machine Theory 178 (2022) 105083. `doi:10.1016/j.mechmachtheory.2022.105083`.
- [19] T. Liu, G. Hao, Design of deployable structures by using bistable compliant mechanisms, Micromachines 13 (5) (2022). `doi:10.3390/mi13050651`.
- [20] G. Chen, Y. Gou, A. Zhang, Synthesis of Compliant Multistable Mechanisms Through Use of a Single Bistable Mechanism, Journal of Mechanical Design 133 (8) (2011). `doi:10.1115/1.4004543`.
- [21] G. C. Yanjie Gou, L. L. Howell, A design approach to fully compliant multistable mechanisms employing a single bistable mechanism, Mechanics Based Design of Structures and Machines 49 (7) (2021). `doi:10.1080/15397734.2019.1707685`.
- [22] A. Rafsanjani, D. Pasini, Bistable auxetic mechanical metamaterials inspired by ancient geometric motifs, Extreme Mechanics Letters 9 (2016). `doi:10.1016/j.eml.2016.09.001`.
- [23] H. Yang, L. Ma, 1D to 3D multi-stable architected materials with zero poisson's ratio and controllable thermal expansion, Materials Design 188 (2020) 108430. `doi:10.1016/j.matdes.2019.108430`.
- [24] S. Chen, X. Liu, J. Hu, B. Wang, M. Li, L. Wang, Y. Zou, L. Wu, Elastic architected mechanical metamaterials with negative stiffness effect for high energy dissipation and low frequency vibration suppression, Composites Part B: Engineering 267 (2023) 111053. `doi:10.1016/j.compositesb.2023.111053`.
- [25] H. Yang, L. Ma, Multi-stable mechanical metamaterials by elastic buckling instability, Journal of materials science 54 (2019) 3509–3526. `doi:10.1007/s10853-018-3065-y`.
- [26] A. Rafsanjani, A. Akbarzadeh, D. Pasini, Snapping mechanical metamaterials under tension, Advanced Materials 27 (39) (2015) 5931–5935. `doi:10.1002/adma.201502809`.
- [27] L. Jin, R. Khajehtourian, J. Mueller, A. Rafsanjani, V. Tournat, K. Bertoldi, D. M. Kochmann, Guided transition waves in multistable mechanical metamaterials, Proceedings of the National Academy of Sciences 117 (5) (2020) 2319–2325. `doi:10.1073/pnas.1913228117`.
- [28] B. Camescasse, A. Fernandes, J. Pouget, Bistable buckled beam and force actuation: Experimental validations, International Journal of Solids and Structures 51 (9) (2014) 1750–1757. `doi:10.1016/j.ijsolstr.2014.01.017`.
- [29] P. Bilancia, G. Berselli, An overview of procedures and tools for designing nonstandard beam-based compliant mechanisms, Computer-Aided Design 134 (2021) 103001. `doi:10.1016/j.cad.2021.103001`.
- [30] L. U. Odhner, A. M. Dollar, The Smooth Curvature Model: An Efficient Representation of Euler–Bernoulli Flexures as Robot Joints, IEEE Transactions on Robotics 28 (4) (2012) 761–772. `doi:10.1109/TRO.2012.2193232`.
- [31] L. L. Howell, A. Midha, T. W. Norton, Evaluation of Equivalent Spring Stiffness for Use in a Pseudo-Rigid-Body Model of Large-Deflection Compliant Mechanisms, Journal of Mechanical Design 118 (1) (1996) 126–131. `doi:10.1115/1.2826843`.
- [32] S. Sen, Beam constraint model: Generalized nonlinear closed-form modeling of beam flexures for flexure mechanism design., Ph.D. thesis, University of Michigan (2013).
URL https://deepblue.lib.umich.edu/handle/2027.42/97856
- [33] S. Sen, S. Awtar, A Closed-Form Nonlinear Model for the Constraint Characteristics of Symmetric Spatial Beams, Journal of Mechanical Design 135 (3) (2013) 031003. `doi:10.1115/1.4023157`.
- [34] G. L. Holst, G. H. Teichert, B. D. Jensen, Modeling and Experiments of Buckling Modes and Deflection of Fixed-Guided Beams in Compliant Mechanisms, Journal of Mechanical Design 133 (5) (2011) 051002. `doi:10.1115/1.4003922`.
- [35] A. Saxena, S. N. Kramer, A Simple and Accurate Method for Determining Large Deflections in Compliant Mechanisms Subjected to End Forces and Moments, Journal of Mechanical Design 120 (3) (1998) 392–400. `doi:10.1115/1.2829164`.
- [36] S. M. Lyon, L. L. Howell, A Simplified Pseudo-Rigid-Body Model for Fixed-Fixed Flexible Segments, International Design Engineering Technical Conferences and Computers and Information in Engineering Conference, 2002, pp. 23–33. `doi:10.1115/DETC2002/MECH-34203`.
- [37] H.-J. Su, A Pseudorigid-Body 3R Model for Determining Large Deflection of Cantilever Beams Subject to Tip Loads, Journal of Mechanisms and Robotics 1 (2) (2009) 021008. `doi:10.1115/1.3046148`.
- [38] G. Chen, B. Xiong, X. Huang, Finding the optimal characteristic parameters for 3R pseudo-rigid-body model using an improved particle swarm optimizer, Precision Engineering 35 (3) (2011) 505–511. `doi:10.1016/j.precisioneng.2011.02.006`.

[39] V. K. Venkiteswaran, H.-J. Su, A Versatile 3R Pseudo-Rigid-Body Model for Initially Curved and Straight Compliant Beams of Uniform Cross Section, Journal of Mechanical Design 140 (9) (2018) 092305. doi:10.1115/1.4040628.

[40] Y.-Q. Yu, Z.-L. Feng, Q.-P. Xu, A pseudo-rigid-body 2R model of flexural beam in compliant mechanisms, Mechanism and Machine Theory 55 (2012) 18–33. doi:10.1016/j.mechmachtheory.2012.04.005.

[41] Y.-Q. Yu, S.-K. Zhu, 5r pseudo-rigid-body model for inflection beams in compliant mechanisms, Mechanism and Machine Theory 116 (2017) 501–512. doi:10.1016/j.mechmachtheory.2017.06.016.

[42] M. Jin, Z. Yang, C. Ynchausti, B. Zhu, X. Zhang, L. L. Howell, Large-Deflection Analysis of General Beams in Contact-Aided Compliant Mechanisms Using Chained Pseudo-Rigid-Body Model, Journal of Mechanisms and Robotics 12 (3) (2020) 031005. doi:10.1115/1.4045425.

[43] L. Qiu, C. Li, S. Dai, Y. Yu, Research on the line-arc-line constant-torque flexure hinge (LAL-CTFH) based on improved pseudo-rigid-body model (PRBM), Mechanism and Machine Theory 174 (2022) 104878. doi:10.1016/j.mechmachtheory.2022.104878.

[44] S. Dai, L. Qiu, Y. Yu, C. Li, On the numerical synthesis of a contact-aided branch hinge (CABH) with variable stiffness, Mechanism and Machine Theory 180 (2023) 105167. doi:10.1016/j.mechmachtheory.2022.105167.

[45] L. Qiu, S. Dai, Y. Li, C. Li, Design and analysis of a contact-aided leaf hinge (CALH) with continuous variable stiffness, Mechanism and Machine Theory 169 (2022) 104653. doi:10.1016/j.mechmachtheory.2021.104653.

[46] G. Chen, F. Ma, Kinetostatic Modeling of Fully Compliant Bistable Mechanisms Using Timoshenko Beam Constraint Model, Journal of Mechanical Design 137 (2) (2015) 022301. doi:10.1115/1.4029024.

[47] P. Liu, P. Yan, Kinetostatic modeling of bridge-type amplifiers based on timoshenko beam constraint model, International Journal of Precision Engineering and Manufacturing 19 (2018) 1339–1345. doi:10.1007/s12541-018-0158-0.

[48] F. Ma, G. Chen, Bi-BCM: A Closed-Form Solution for Fixed-Guided Beams in Compliant Mechanisms, Journal of Mechanisms and Robotics 9 (1) (2016) 014501. doi:10.1115/1.4035084.

[49] P. Bilancia, M. Baggetta, G. Hao, G. Berselli, A variable section beams based Bi-BCM formulation for the kinetostatic analysis of cross-axis flexural pivots, International Journal of Mechanical Sciences 205 (2021) 106587. doi:10.1016/j.ijmecsci.2021.106587.

[50] L. Meng, R. Kang, D. Gan, G. Chen, L. Chen, D. T. Branson, J. S. Dai, A Mechanically Intelligent Crawling Robot Driven by Shape Memory Alloy and Compliant Bistable Mechanism, Journal of Mechanisms and Robotics 12 (6) (2020) 061005. doi:10.1115/1.4046837.

[51] J. Zhu, G. Hao, H. Tang, Design and Modelling of a Generic Compliant Mechanism with Bi-stability and Static Balancing, in: 2022 IEEE International Conference on Manipulation, Manufacturing and Measurement on the Nanoscale (3M-NANO), 2022, pp. 172–177. doi:10.1109/3M-NANO56083.2022.9941512.

[52] G. Hao, Extended nonlinear analytical models of compliant parallelogram mechanisms: third-order models, Transactions of the Canadian Society for Mechanical Engineering 39 (1) (2015) 71–83. doi:10.1139/tcsme-2015-0006.

[53] J. Zhu, G. Hao, Modelling of a general lumped-compliance beam for compliant mechanisms, International Journal of Mechanical Sciences (2023) 108779doi:10.1016/j.ijmecsci.2023.108779.

[54] M. Ling, L. Yuan, X. Zhang, Geometrically nonlinear analysis of compliant mechanisms using a dynamic beam constraint model (DBCM), Mechanism and Machine Theory 191 (2024) 105489. doi:10.1016/j.mechmachtheory.2023.105489.

[55] F. Ma, G. Chen, Modeling Large Planar Deflections of Flexible Beams in Compliant Mechanisms Using Chained Beam-Constraint-Model, Journal of Mechanisms and Robotics 8 (2) (2015) 021018. doi:10.1115/1.4031028.

[56] G. Chen, F. Ma, G. Hao, W. Zhu, Modeling Large Deflections of Initially Curved Beams in Compliant Mechanisms Using Chained Beam Constraint Model, Journal of Mechanisms and Robotics 11 (1) (2018) 011002. doi:10.1115/1.4041585.

[57] P.-L. Chang, I.-T. Chi, N. D. K. Tran, D.-A. Wang, Design and modeling of a compliant gripper with parallel movement of jaws, Mechanism and Machine Theory 152 (2020) 103942. doi:10.1016/j.mechmachtheory.2020.103942.

[58] F. Ma, G. Chen, H. Wang, Large-Stroke Constant-Force Mechanisms Utilizing Second Buckling Mode of Flexible Beams: Evaluation Metrics and Design Approach, Journal of Mechanical Design 142 (10) (2020) 103303. doi:10.1115/1.4046242.

[59] K. Kong, G. Chen, G. Hao, Kinetostatic Modeling and Optimization of a Novel Horizontal-Displacement Compliant Mechanism, Journal of Mechanisms and Robotics 11 (6) (2019) 064502. doi:10.1115/1.4044334.

[60] W. Zeng, G. Xu, H. Jiang, C. Huang, F. Gao, S. Yang, Design of a variable-diameter wheel with a novel distributed compliant mechanism, Mechanism and Machine Theory 189 (2023) 105450. doi:10.1016/j.mechmachtheory.2023.105450.

[61] I.-T. Chi, T. H. Ngo, P.-L. Chang, N. D. K. Tran, D.-A. Wang, Design of a bistable mechanism with b-spline profiled beam for versatile switching forces, Sensors and Actuators A: Physical 294 (2019) 173–184. doi:10.1016/j.sna.2019.05.028.

[62] G. Chen, R. Bai, Modeling Large Spatial Deflections of Slender Bisymmetric Beams in Compliant Mechanisms Using Chained Spatial-Beam Constraint Model, Journal of Mechanisms and Robotics 8 (4) (2016) 041011. doi:10.1115/1.4032632.

[63] R. Bai, G. Chen, S. Awtar, Closed-form solution for nonlinear spatial deflections of strip flexures of large aspect ratio considering second order load-stiffening, Mechanism and Machine Theory 161 (2021) 104324. doi:10.1016/j.mechmachtheory.2021.104324.

[64] B. Todd, B. D. Jensen, S. M. Schultz, A. R. Hawkins, Design and Testing of a Thin-Flexure Bistable Mechanism Suitable for Stamping From Metal Sheets, Journal of Mechanical Design 132 (7) (2010) 071011. doi:10.1115/1.4001876.

[65] J. Zhao, J. Jia, X. He, H. Wang, Post-buckling and Snap-Through Behavior of Inclined Slender Beams, Journal of Applied Mechanics 75 (4) (2008) 041020. doi:10.1115/1.2870953.

[66] A. Zhang, G. Chen, A Comprehensive Elliptic Integral Solution to the Large Deflection Problems of Thin Beams in Compliant Mechanisms, Journal of Mechanisms and Robotics 5 (2) (2013) 021006. doi:10.1115/1.4023558.

[67] N. Iwatsuki, T. Kosaki, Large deformation analysis and synthesis of elastic closed-loop mechanism made of a certain spring wire described by free curves, Chinese Journal of Mechanical Engineering 28 (2015) 756–762. doi:10.3901/CJME.2015.0506.067.

[68] P. Kuresangsai, M. O. T. Cole, G. Hao, Grasp stability and design analysis of a flexure-jointed gripper mechanism via efficient energy-based modeling, IEEE Robotics and Automation Letters 7 (4) (2022) 12499–12506. doi:10.1109/LRA.2022.3220152.

[69] O. A. Turkkan, H.-J. Su, A general and efficient multiple segment method for kinetostatic analysis of planar compliant mechanisms, Mechanism and Machine Theory 112 (2017) 205–217. doi:https://doi.org/10.1016/j.mechmachtheory.2017.02.010.

[70] S. Wu, Z. Shao, H. Su, H. Fu, An energy-based approach for kinetostatic modeling of general compliant mechanisms, Mechanism and

Machine Theory 142 (2019) 103588. doi:https://doi.org/10.1016/j.mechmachtheory.2019.103588.

[71] G. Chen, F. Ma, R. Bai, W. Zhu, S. P. Magleby, L. L. Howell, An Energy-Based Framework for Nonlinear Kinetostatic Modeling of Compliant Mechanisms Utilizing Beam Flexures, Journal of Computing and Information Science in Engineering 21 (6) (2021) 064501. doi:10.1115/1.4050472.

[72] R. V. Southwell, Castigliano's principle of minimum strain-energy, Proceedings of the Royal Society of London. Series A - Mathematical and Physical Sciences 154 (881) (1936) 4–21. doi:10.1098/rspa.1936.0033.

[73] A. Bhrawy, E. Doha, S. Ezz-Eldien, M. Abdelkawy, A numerical technique based on the shifted legendre polynomials for solving the time-fractional coupled kdv equations, Calcolo 53 (2016) 1–17. doi:10.1007/s10092-014-0132-x.

[74] R. T. Rockafellar, Lagrange multipliers and optimality, SIAM Review 35 (2) (1993) 183–238. doi:10.1137/1035044.

[75] D. Spring, On the second derivative test for constrained local extrema, The American Mathematical Monthly 92 (9) (1985) 631–643. doi:10.2307/2323709.

[76] H. Karabulut, The physical meaning of Lagrange multipliers, European Journal of Physics 27 (4) (2006) 709. doi:10.1088/0143-0807/27/4/003.

[77] T. J. Ypma, Historical Development of the Newton–Raphson Method, SIAM Review 37 (4) (1995) 531–551. doi:10.1137/1037125.

[78] J. Verbeke, R. Cools, The Newton-Raphson method, International Journal of Mathematical Education in Science and Technology 26 (2) (1995) 177–193. doi:10.1080/0020739950260202.

[79] UltiMaker, UltiMaker Tough PLA Technical data sheet, Accessed on 30th, November, 2023 (5 2022).
URL https://support.makerbot.com/s/article/1667411002379

[80] L. Mendo, Estimation of a probability with guaranteed normalized mean absolute error, IEEE Communications Letters 13 (11) (2009) 817–819. doi:10.1109/LCOMM.2009.091128.

[81] Y. K. Yong, T.-F. Lu, Kinetostatic modeling of 3-rrr compliant micro-motion stages with flexure hinges, Mechanism and Machine Theory 44 (6) (2009) 1156–1175. doi:https://doi.org/10.1016/j.mechmachtheory.2008.09.005.

[82] A new pseudo-rigid-body model approach for modeling the quasi-static response of planar flexure-hinge mechanisms, Mechanism and Machine Theory 124 (2018) 150–161. doi:https://doi.org/10.1016/j.mechmachtheory.2018.02.011.

[83] J. Wu, Y. Zhang, S. Cai, J. Cui, Modeling and analysis of conical-shaped notch flexure hinges based on nurbs, Mechanism and Machine Theory 128 (2018) 560–568. doi:https://doi.org/10.1016/j.mechmachtheory.2018.07.005.

[84] S. Awtar, Synthesis and analysis of parallel kinematic xy flexure mechanisms, Ph.D. thesis, Massachusetts Institute of Technology (2003).

[85] G. Hao, H. Li, S. Kemalcan, G. Chen, J. Yu, Understanding coupled factors that affect the modelling accuracy of typical planar compliant mechanisms , Frontiers of Mechanical Engineering 11 (2016) 129–134. doi:10.1007/s11465-016-0392-z.